CN-164660

SANDIA REPORT

Feasibility of Flight Experiments and Instrumentation Hardware for In-Flight Hypersonic Boundary-Layer Measurements

R. J. Cattolica, R. L. Schmitt, R. E. Palmer

FEASIBILITY OF FLIGHT EXPERIMENTS AND INSTRUMENTATION HARDWARE FOR IN-FLIGHT HYPERSONIC BOUNDARY-LAYER MEASUREMENTS*

R. J. Cattolica, R. L. Schmitt, and R. E. Palmer

Combustion Research Facility

Sandia National Laboratories

Livermore, CA 94551-0969

ABSTRACT

We have examined the feasibility of implementing nonintrusive optical diagnostics to measure the properties of the boundary layer surrounding a hypersonic vehicle. Measurements of density, temperature, location of the shock front, and N_2, O_2, and NO concentrations are feasible using electron-beam fluorescence, for which instrumentation appropriate for flight experiments already exists. In particular, NO will be a key indicator of the chemistry occurring at the vehicle nose and leading edges. Measurements of velocity and O_2 and NO concentrations will be feasible using laser-induced fluorescence when rugged and reliable miniature uv laser sources become available; such laser sources should be developed in the next few years. Optical and sensor instrumentation for spectrally resolving the fluorescence along a line emanating from the vehicle and passing radially through the shock front is presently available. Laboratory and wind tunnel experiments will be required to develop the technology base needed to apply these advanced diagnostics. Nevertheless, experimental data acquired from these diagnostic methods, both in flight experiments and in wind tunnel tests, will be invaluable for validating computational fluid dynamics computer codes and for designing next-generation high-performance hypersonic flight vehicles.

CONTENTS

[NOTE: This report has been extracted from a larger feasibility study examining various aspects of in-flight experiments to measure boundary layer properties around a hypersonic vehicle. Sections 7.0 and 7.2 focus on the feasibility of specific diagnostic techniques, primarily electron-beam and laser-induced fluorescence, and the hardware required to implement these diagnostic methods. Information on the larger feasibility study, which examines flight profiles and other considerations in addition to diagnostic techniques, can be obtained from George F. Wright Jr., Org. 9142.]

7.0 Flight Experiment Study and Evaluation

<u>Introduction</u>

The properties of the hypersonic boundary layer surrounding a transatmospheric vehicle are strongly influenced by the shock wave at the leading edge of the vehicle. Below 60 km altitude, a viscous shock layer model[1] can be used to determine the gas temperature, velocity, density, and species composition through the shock. Using these properties as initial conditions, a boundary-layer calculation[2] can predict the development and structure of the hypersonic flow near the surface of a typical transatmospheric vehicle. The boundary-layer characteristics for an 8° sphere-cone body at Mach 21 and at an altitude of 55 km are listed in Table 7.0.1. At altitudes above 60 km, computational fluid dynamics (CFD) methods assuming thin shocks and equilibrated internal energy begin to fail. At these higher altitudes the direct simulation Monte Carlo (DSMC) technique becomes effective. Recent calculations[3] for a 5° cone using the DSMC technique give results similar to those listed in Table 7.0.1. In addition, DSMC models predict the nonequilibrium distribution of internal energy, as well as translational, rotational, and vibrational temperatures.

When examining the feasibility of advanced optical diagnostics for in-flight experiments, we will use the nominal boundary-layer properties listed in Table 7.0.1. At higher altitudes, the most significant changes will be the overall lowering of density, thickening of the boundary layer, and departure of internal temperatures from equilibrium. In general, the impact of higher altitude will be to decrease optical signal levels. Compensation for this effect can be made by increasing signal acquisition times and by using higher power excitation sources. For flight experiments, data-acquisition times and available on-board power will be limited, so that optical diagnostics producing strong signal levels, such as laser-induced and electron-beam fluorescence, are recommended for the measurement of hypersonic boundary-layer flow-field properties. These measurements are essential to validate current CFD methods for predicting hypersonic fluid dynamics.

Density: The density distribution across the boundary layer can be measured using electron-beam excitation of the nitrogen molecule. By measuring the fluorescence signal from the N_2^+ ion, number densities up to 10^{16} cm^{-3} have been measured, with a linear dependence of signal on density. At higher number densities, the relationship becomes

7

nonlinear. This technique has not been tested at the high gas temperatures (>500 K) in the hypersonic boundary layer and will require laboratory development.

Velocity: A new technique that uses a pulsed electron beam to form a packet of N_2^+ ions and a pulsed laser to excite fluorescence from the ions at a downstream location can provide a velocity measurement using a simple transit-time approach. Combining this technique with a linear displacement photodiode detector can provide the capability to profile the velocity across the hypersonic boundary layer. This approach has been demonstrated in low-density hypersonic flows with an ion probe to measure time of flight. Laser-induced fluorescence excitation and spatial imaging of the fluorescence have not yet been attempted and will require laboratory development.

Temperature: Rotational and vibrational temperature measurements can be obtained with the electron-beam fluorescence technique. N_2 rotational temperature measurements up to 400 K at number densities up to 10^{16} cm^{-3} have been demonstrated. The measurement of rotational temperatures above 400 K will require model development and laboratory experiments. Vibrational temperature measurements at the high temperatures expected in the boundary layer have also not yet been attempted, and they will require laboratory development and modeling. Using image-intensified charge-coupled device (CCD) cameras combined with a miniature spectrograph, spatial profiling of the rotational and vibrational temperature through the boundary layer can be obtained.

Minor Species: The measurement of minor species is important for understanding the role of nonequilibrium temperatures and chemistry in transatmospheric flight. For high-altitude hypersonic flight, the structure of the viscous, nonequilibrium shock layer at the nose or leading edge of a body will have a significant effect on the high-temperature air composition. The formation of minor species such as O, N, and NO will be sensitive to the temperature and density distribution through the shock layer. The NO molecule is the most likely candidate to be measured using single-photon laser-induced fluorescence (LIF) excitation. O-atom and N-atom LIF require a two-photon excitation process, necessitating a more complex laser system. Nitric oxide (NO) concentration measurements have been made in flames at number densities of 10^{13} cm^{-3} and temperatures up to 2000 K with LIF. The extension of this technique to flight experiments will require the development of a detailed model of laser excitation dynamics that can be used to evaluate LIF excitation schemes with new laser sources.

8

Active probing of the boundary-layer gases with electron-beam or laser excitation, either individually or in combination, for measuring density, velocity, temperature, and species concentrations will be examined in more detail below. The availability of models for data interpretation will also be discussed. In addition, the feasibility of laboratory experiments to evaluate these approaches and to provide necessary data bases will be explored. The flow conditions in the hypersonic boundary layer on an 8° sphere-cone body at Mach 21 and at an altitude of 55 km are used as a nominal basis upon which to make recommendations of suitable optical diagnostics for the flow-field measurements. All the diagnostic techniques that have been identified will require substantial laboratory research to design and interpret eventual flight experiments. We thus begin with a description of a hypersonic free-jet experiment in which diagnostic techniques for flight experiments can be refined. We then describe a new technique for measuring velocity using an ion time-of-flight method. Electron-beam fluorescence is discussed at length for measuring density, vibrational temperature, rotational temperature, and species concentrations in a hypersonic boundary layer. A summary of a program plan for developing advanced optical diagnostics for flight experiments concludes this section.

Hypersonic Free-Jet Experiment

For laboratory studies of the suggested spectroscopic diagnostics, a high-temperature, high-pressure free jet exhausting into vacuum can be used (Fig. 7.0.1). The hypersonic performance of this free-jet source can be changed to obtain different gas conditions. The stagnation temperature and pressure can be varied to obtain different free-stream density, velocity, and temperature. In addition, by using mixtures of nitrogen doped into other inert carrier gases, both the temperature and velocity can be tailored to specific needs. As an example of this versatility, the hypersonic limiting velocity of mixtures of nitrogen in helium are plotted in Fig. 7.0.2 as a function stagnation temperature. For a 2% nitrogen-doped helium mixture, velocities up to 5 km/s can be obtained. This is equivalent to to 75% of the the flight velocity at Mach 21 at 55 km altitude.

The hypersonic flow that can be produced with this free-jet source is ideally suited for the development of diagnostic techniques for flight research. Using electron-beam-excited fluorescence from N_2 on the centerline of the hypersonic free jet, the spectroscopic codes required to extract density and temperature measurements can be verified. The density and rotational temperature measurement techniques from N_2^+ fluorescence are well

established at low temperatures (< 290 K); however, at high temperature both rotational and vibrational temperature measurement techniques need substantial development. The measurement of gas velocity based on the formation of the N_2^+ ion with a pulsed electron beam followed by time-of-flight (TOF) detection with laser-induced fluorescence (LIF) using a pulsed laser can also be evaluated by crossing the two beams on the centerline of the free jet, as depicted in Fig. 7.0.1, and measuring the hypersonic velocity. A similar approach can be used for an in-flight measurement and is also depicted in Fig. 7.0.1. By doping nitrogen with nitric oxide, measurements of the excitation dynamics, collisional quenching, and spectral characteristics can be studied under conditions in which the rotational and vibrational temperatures can be substantially different. This type of nonequilibrium energy distribution can be expected to be encountered in actual flight experiments. For studies at higher temperature under equilibrium conditions, a nitric oxide-doped low-pressure hydrogen-oxygen flame can also be used.

Velocity Measurement by Ion Time-of-Flight (TOF)

The development of an ion TOF technique (based on ion detection with a biased probe) for the measurement of gas for low-density wind tunnel applications was evaluated for NASA by the University of California at Berkeley over 30 years ago.[4] The conclusion of that report was that the required temporal resolution was difficult to obtain because of the spatial and temporal width of the pulsed electron beam used to form the ion packet, subsequent broadening during transit, and difficulty in determining the exact time of arrival from the current collected with the ion probe. These limitations were overcome some twenty years later at the DFVLR in Göttingen, Germany,[5,6] where hypersonic velocities up to 2 km/s were measured, and at the University of Paris.[7] The German experiment required an ion flight path of 37.5 cm to attain 1% accuracy. The temporal resolution in the experiment was 100 ns. This flight-path distance is not practical for either in-flight research or laboratory studies with the free-jet source. However, the flight path length can be decreased in proportion to the improvement in temporal resolution. The use of a pulsed electron beam of short duration (<<1 μs), and detection with a pulsed laser can provide the required improvement in temporal resolution.

As stated previously, the accuracy of a TOF velocity determination based on the electron beam/LIF detection scheme will depend on the spatial limitation on the flight path length and the temporal resolution in measuring the time of arrival. The velocity v in a

time-of-flight experiment is calculated simply from the the flight time t and the flight distance d:

$$v = d/t. \qquad (7.0.1)$$

For a given maximum relative error in the velocity $\delta v/v$, the required temporal resolution of the time-of-flight measurement δt is given by:

$$\delta t = (\delta v/v) \, d/v. \qquad (7.0.2)$$

Eq. 7.0.2 implies that the required temporal resolution for a given accuracy in velocity is proportional to the distance over which the time of flight is measured and inversely proportional to the velocity. In Fig. 7.0.3 curves are plotted of the required time resolution for a 1% accuracy in the velocity measurement as a function of velocity. The curves are parameterized by time-of-flight path lengths of 0.1, 1, and 10 cm.

The hypersonic free jet considered for diagnostic development is scaled by the 1-mm diameter of the orifice exhausting gas from the high-pressure stagnation chamber. A reasonable electron-beam/laser-beam separation distance for the TOF velocity measurement would be 2 mm. For a gas velocity of 2 km/s, the resulting flight time would be 1 μs. The required temporal resolution taken from Fig. 7.0.3 for a velocity measurement accurate to ±1% would be 10 ns. Using a commercially available pulsed electron beam, a pulse width of 10 ns and spatial resolution of 0.5 mm is possible. For flight experiments, the gas velocity could be as high as 8 km/s. A flight path of 20 mm increases the minimum temporal resolution to 25 ns. If a pulsed nitrogen laser is used to excite fluorescence for the ion detection, the detection resolution should be less than 1 ns.

Another consideration relative to the temporal requirements of an ion-tracer TOF measurement is the lifetime of the ion. For the N_2^+ ion formed by a pulsed electron beam in the low-density, high-temperature environment of the hypersonic boundary layer, the ion removal is governed by charge exchange[8] with the oxygen molecule:

$$N_2^+ + O_2 \xrightarrow{k_1} O_2^+ + N_2, \qquad (7.0.3)$$

where the rate constant k_1 is $2 \cdot 10^{-11}$ cm^3/s at 1000 K, and by dissociative recombination with the electrons[9] in the plasma formed by the electron beam:

$$N_2^+ + e \xrightarrow{k_2} N + N. \qquad (7.0.4)$$

Here, k_2 is $\sim 10^{-7}$ cm^3/s. For charge exchange with O_2, the rate of decrease of N_2^+ ions is:

$$\frac{d[N_2^+]}{dt} = -k_1[N_2^+][O_2]. \qquad (7.0.5)$$

The concentration of N_2^+ at a given time after formation by the pulsed electron beam is obtained by integrating Eq. 7.0.5 and is:

$$\frac{N_2^+(t)}{N_2^+(0)} = \exp(-k_1[O_2]t). \qquad (7.0.6)$$

The time required for charge exchange with molecular oxygen to reduce the ion concentration to 1/e of it original value $N_2^+(0)$ is:

$$t_{O_2} = (k_1[O_2])^{-1}. \qquad (7.0.7)$$

Since the O_2 concentration on a mole-fraction basis is nearly constant and independent of altitude, it is directly proportional to the atmospheric density. The value of the ion lifetime due to charge exchange with molecular oxygen is given as a function of ambient air number density in Fig. 7.0.4. At an atmospheric density of 10^{16} cm^{-3}, the ion lifetime is 25 μs and the charge transfer mechanism for loss of N_2^+ should not affect the signal level in the TOF velocity measurement in the laboratory simulation or the in-flight experiment.

The rate of ion loss due to dissociative recombination from Eq. 7.0.4 is:

$$\frac{d[N_2^+]}{dt} = -k_2[N_2^+][e]. \qquad (7.0.8)$$

12

Since the overall plasma formed by the pulsed electron beam must be neutral, the electron concentration is essentially equal to that of the ion, $[e] = [N_2^+]$, so that Eq. 7.0.8 becomes:

$$\frac{d[N_2^+]}{dt} = -k_2 [N_2^+]^2 .$$

(7.0.9)

Integrating Eq. 7.0.9 analytically yields the relation:

$$N_2^+(t) = \frac{N_2^+(0)}{N_2^+(0) k_2 t + 1} .$$

(7.0.10)

The time for N_2^+ to be reduced to $1/e$ of its initial value by recombination is:

$$t_e = \frac{1.72}{N_2^+(0) k_2} .$$

(7.0.11)

The initial ionization fraction of the nitrogen molecule is calculated to be 10^{-7} for a 10-ns pulsed electron beam operating at 10 kV and 1 mA with a 0.5-mm beam diameter, independent of gas density. This assumption of a linear ionization fraction is valid for nitrogen up to a density of 10^{16} cm^{-3}. The ion lifetime from removal by recombination is two orders of magnitude longer than the lifetime from charge transfer (Fig. 7.0.4). At a density of 10^{16} cm^{-3}, the 25-μs lifetime based on charge transfer, which determines the overall lifetime, would have little effect on either the free-jet experiment or flight experiments at velocities greater than 90 m/sec.

Electron-Beam Fluorescence

The electron-beam fluorescence (EBF) technique[10] was developed in the 1960's as a spectroscopic method for determining gas density, velocity, and temperature at low density ($<10^{16}$ cm^{-3}). The EBF technique became a viable research tool in the early 1970's as a diagnostic for low-density hypersonic wind tunnel studies of gas dynamic[11] and aerodynamic phenomena.[12] Except for a few applications in the study of aerodynamic isotope separation schemes[13] in the late 1970's, however, the EBF technique has had few applications in hypersonics. In addition, primarily because of lack of support, little effort

has been made to apply advanced electro-optic instrumentation developed in the last decade to the EBF technique.

In considering the EBF technique for hypersonic flight research, it is necessary to examine the implications of the high-temperature (4000 K) and hypervelocity (6 km/s) environment to be encountered. In most of the previous laboratory studies (except for some work in heated-flow facilities), EBF has been used at gas temperatures significantly below ambient conditions (293 K). In the following sections, the measurement of density and rotational and vibrational temperatures using EBF are discussed in the context of the high-enthalpy environment of hypersonic flight. We assume in the following discussion the nominal boundary-layer characteristics of an 8° sphere-cone body at an altitude of 55 km and at Mach 21.

Density: Measurements of nitrogen density up to 10^{16} cm^{-3} have been demonstrated routinely with EBF in laboratory studies of hypersonic flows. At temperatures <1000 K, the fluorescence signal from the (0,0) band of the $B^2\Sigma - X^2\Sigma$ transition of the N_2^+ ion is proportional to the N_2 number density when normalized to the electron beam current. The cross-section for electron-beam excitation[14] of this band is relatively small at 10 keV (1.5 • 10^{-18} cm^2) and decreases with increasing electron beam energy. For densities up to 10^{16} cm^{-3}, quenching effects are not important, and no quenching correction is necessary. In the wind tunnel studies in which EBF has been used, either the gas temperature was sufficiently low that only the first vibrational level was populated, or the density was not high enough to allow relaxation of the upper vibrational levels. In either case, the ground-state vibrational population fraction was constant, so that the relationship of the EBF signal to gas density was explicit.

For high-enthalpy hypersonic flight conditions, the vibrational-population distribution in nitrogen will reflect the change in vibrational temperature due to shock heating of the gas and subsequent vibrational energy transfer. In Fig. 7.0.5, the relative vibrational-population distribution for nitrogen is shown as a function of temperature. Above 1000 K, the population of the first vibrational level begins to change significantly due to energy redistribution and becomes a function of temperature. A density measurement based on the EBF technique using this first vibrational level will therefore depend on the vibrational temperature, particularly at the elevated temperatures encountered in hypersonic flight. This will require that the fluorescence measurement from the (0,0) band be accompanied by a simultaneous measurement of the vibrational-population

distribution in higher vibrational levels to determine the density in a hypersonic boundary layer.

Vibrational Temperature: The vibrational energy distribution in the nitrogen molecule at elevated temperature can be measured[15] by observing the relative EBF intensities from specific vibrational emission bands (v',v") in the $B^2\Sigma(v') - X^2\Sigma(v")$ electronic transition of the N_2^+ ion. The emission intensity $I_{v'v"}$ is given by the following relation:

$$I_{v'v"} = \frac{C\, v_{v'v"}^4\, q(v';v")\, \sum\limits_{v_0"} \left[n(v_0")\, q(v';v_0") \right]}{\sum\limits_{v'} \left[v_{v'v"}^3\, q(v';v") \right]}, \qquad (7.0.12)$$

where C is constant and q(v',v") is the Franck-Condon factor for the $B^2\Sigma(v') - X^2\Sigma(v")$ transition at the emission frequency $v_{v'v"}$. The bracketed expression in the numerator of Eq. 7.0.12 describes the electron-beam excitation rate of the population of the vibrational level v' in terms of the Franck-Condon factors $q(v',v_0")$ connecting the B(v') state of the N_2^+ ion and the various vibrational levels $v_0"$ in the ground electronic state $X^2\Sigma(v_0")$ of the nitrogen molecule. The term $n(v_0")$ is the number density in the vibrational level $v_0"$ and reflects the vibrational energy distribution in the nitrogen molecule. The bracketed term in the denominator of Eq. 7.0.12 is the total radiative depopulation rate from the v' level in the B state of the N_2^+ ion.

The Franck-Condon factors used to model the EBF excitation process can be calculated using appropriate intermolecular potentials.[16] The Franck-Condon factors for emission can be calculated from band intensity data in the literature.[17] Eq. 7.0.12 can also be reformulated in terms of vibrational line strengths, taking into account the variation in the electronic transition moment with vibrational levels, to obtain a more rigorous solution.

In Table 7.0.2, the strong vibrational emission bands in the $B^2\Sigma(v') - X^2\Sigma(v")$ transition in the N_2^+ ion are listed along with the transition wavelength and the radiative lifetime[16] of the upper state in the transition. The radiative lifetimes for all of these transitions are short enough so that with a quenching cross-section[10] of $1.5 \cdot 10^{-16}$ cm^2, quenching is not a significant depopulation process until the gas density exceeds 10^{16} cm^{-3}. At hypervelocity conditions (~10 km/s), the radiation from these bands is convected by the

fluid motion at most only 1.0 mm from the electron-beam excitation source. The design of a light-collection system with apertured detectors in an actual flight experiment is made much simpler because of this limited convection of the radiation.

Using Eq. 7.0.12 and the appropriate parameters for the transitions listed in Table 7.0.2, the relative signal strengths for the vibrational-band emission from the EBF are plotted as a function of vibrational temperature in Fig. 7.0.6. The (0,0) band at 391.4 nm is the strongest feature in the $B^2\Sigma(v') - X^2\Sigma(v'')$ system. The emission strength of this band at 300 K is used to normalize all of the emission signals in Fig. 7.0.6. We assume a uniform detector sensitivity for the detection of each emission band.

The decrease in the (0,0) band signal with increasing temperature seen in Fig. 7.0.6 results from the redistribution of vibrational population to other high vibrational levels, as indicated in Fig. 7.0.5. This effect is not significant for vibrational temperatures below 1000 K. The (0,1) band follows the behavior of the (0,0) band directly, but with a factor-of-three less signal. The (1,0) band has a finite signal strength (6%) even at 300 K, where the population of the v" level in the N_2 molecule is virtually empty. This (1,0) band strength results from electron-beam excitation from $v_0''=0$ to $v'=1$. As the vibrational temperature is increased, the (1,0) band signal strength increases as population in the $v_0''=1$ level increases, and the more favorable Franck-Condon factor $q(v'=1,v_0''=1)$ for electron-beam excitation into the $v'=1$ level in the nitrogen ion becomes the dominate excitation path. At 1000 K the (2,1) band begins to appear in the spectrum, and above 2000 K the (3,2) band becomes significant. At high temperature (5000 K), all the bands except (0,0) have signal levels within a factor of two of each other.

To determine the vibrational temperature (T_v) of the nitrogen molecule, the ratios of the vibrational-band emission intensities can be used. In Fig. 7.0.7, ratios of the (1,0), (2,1), and (3,2) bands compared to the (0,1) band are plotted as a function of vibrational temperature. The (0,0) band was not considered because it will probably be used for a rotational-temperature measurement in an actual flight experiment. For nitrogen gas in vibrational equilibrium, any of these curves could be used. However, because of the shapes of the curves, each vibrational-band intensity ratio curve has a range of temperature over which it is more sensitive to temperature. For the I(0,1)/I(1,0) band ratio, this temperature range is 1000 to 2000 K, for I(0,1)/I(2,1) the range is 2000 to 3500 K, and for I(0,1)/I(3,2) the range is 3500 to 5000 K. Evaluation of this approach for making

vibrational temperature measurements has been very limited because of the difficulty in producing vibrationally equilibrated gas at these high temperatures.

If the gas is not in thermal equilibrium, then the vibrational-population distribution must be determined directly by measuring all of the band intensities listed in Table 7.0.2. By writing Eq. 7.0.12 for each band, a truncated set of algebraic equations can be solved for the vibrational-population distribution. An equivalent vibrational temperature can be determined by taking moments of the distribution function. In an actual flight experiment, nonequilibrium vibrational conditions should be expected, and this latter approach will probably be necessary. This will require laboratory studies of vibrationally hot nitrogen gas that is not in thermal equilibrium to test the above spectroscopic data analysis scheme.

Rotational Temperature: Techniques to obtain rotational temperatures of nitrogen using EBF were developed extensively in the 1960's and early 1970's for low-density wind tunnel applications. The original description by Muntz[15] assumed that the electron-excitation process followed dipole optical selection rules. This approach was evaluated by numerous researchers and has been found to be an adequate model for temperature measurements near ambient temperature (293 K). For lower temperature applications (<150 K), higher order corrections have been applied to explain the overpopulation of higher rotational levels. In these lower temperature studies, the assumption of rotational equilibrium was often an issue that confused the interpretation of the rotational spectra and the evaluation of more refined models. A model[18] that incorporates higher order quadrupole transitions to describe the effect of the ejected electron in the EBF excitation process was found to be successful in explaining the non-Boltzmann types of rotational distributions observed under conditions where rotational equilibrium was a valid assumption.

For higher temperature applications (>293 K), no extensive studies of the EBF rotational excitation model have been conducted. Since flight research will undoubtedly involve measurements at high rotational temperatures, laboratory studies will be important in the development of a spectroscopic model for data interpretation. The hypersonic free-jet experiment described earlier is capable of producing vibrationally hot (2500 K) and rotationally cooled (500 to 1000 K) nitrogen gas which could be used to explore the rotational- and vibrational-temperature measurement techniques that have been described here for application to flight research.

17

In developing a design of the instrumentation to measure the rotational temperature, it is useful to calculate the N_2^+ rotational spectrum produced with EBF. The rotational structure of the (0,0) vibrational band fluorescence was calculated using Muntz's original excitation model based on dipole selection rules. In Figs. 7.0.8a-c the rotational spectrum for three different rotational temperatures (300, 600, and 1000 K) are presented. The band head of the (0,0) band is at 391.4 nm, with an R branch below 391.0 nm and a P branch above 391.0 nm. Because the P branch reverses in wavelength as the rotational quantum number K" is increased, the P branch folds over on itself and is difficult to resolve with a spectrograph. The spectra in Figs. 7.0.8a-c are all normalized to the K"=9 rotational line in the P branch, which is the strongest line at 300 K. The R branch of the (0,0) spectrum is dispersed to lower wavelengths as the rotational quantum number K" increases. The factor-of-two variation in alternate P-branch lines is due to an increase in the rotational state degeneracy with odd or even rotational quantum number.

The R branch of the (0,0) band is best suited for rotational-temperature measurements for hypersonic flight conditions. A logarithmic plot of the rotational line intensities (normalized by line strength) vs. rotational energy level yields a straight line whose slope is inversely proportional to temperature for N_2 in rotational equilibrium. For the conditions to be encountered in hypersonic flight, this should be a valid assumption. As the temperature is increased to 600 K, the (0,0) band rotational spectrum shown in Fig. 7.0.8b is spread to lower wavelengths as higher rotational levels become populated. Although the integrated signal strength for the (0,0) vibrational band remains relatively constant as the temperature increases up to 1000 K, the individual rotational transitions are much weaker because the intensity is distributed over more lines (Fig. 7.0.8c). At temperatures above 1000 K, the signal levels in the R branch are reduced even more, and the spectrum is complicated by the appearance of P-branch lines overlapping the R branch. To fully resolve the R branch, a spectrograph with a spectral resolution of 0.030 nm is required. Although coarse resolution and ratios of portions of the P branch could be used, care must be exercised in assuring rotational equilibrium in the system being investigated. Although the rotational temperature in a hypersonic boundary layer will probably be in equilibrium, local shocks could produce nonequilibrium conditions.

The spectra in Fig. 7.0.8 were calculated for a constant number density. For a constant-pressure system, the signal levels in Fig. 7.0.8 would be reduced by a factor proportional to 1/T and would be significantly weaker. Since in hypersonic flight the temperature increase from shock heating is also associated with an increased number

density behind the shock, a constant-pressure assumption would be overly conservative. The constant number density assumption used to calculate the spectra should provide a reasonable estimate of the change in relative signal level with temperature.

Species Concentrations: The measurement of species concentrations was discussed in general terms in the introduction. We present here a more specific discussion of the applicability of laser-induced and electron-beam fluorescence spectroscopy for species concentration measurements. Since the gas composition in a hypersonic boundary layer surrounding a transatmospheric vehicle is strongly influenced by the shock-layer structure at the nose of the vehicle, its detailed measurement provides an excellent test of CFD methods for modeling hypersonic aerothermodynamics. The gas composition for a hypersonic boundary layer on an 8° cone at Mach 21 at an altitude of 55 km predicted from a continuum CFD boundary-layer calculation[2] is given in Table 7.0.1. For altitudes above 60 km, continuum CFD methods, which assume thin shocks and equilibrated internal energy, begin to fail; direct simulation Monte Carlo (DSMC) techniques[3] can be used for these conditions.

The principal major species in a hypersonic boundary layer are molecular oxygen and nitrogen. As discussed above, the electron-beam fluorescence technique is a well established method for the measurement of density of molecular nitrogen under lower density hypersonic conditions at or below 300 K. Since the temperature in a hypersonic boundary layer would be expected to be as much as an order of magnitude higher, laboratory experiments at temperatures exceeding 2000 K are necessary to validate the electron-beam fluorescence concentration measurement. With regard to oxygen, the electron-beam fluorescence technique is complicated by an excitation mechanism that results in fluorescence from O^+,[19] O^{++} (380-480 nm),[20] and from the first negative system $O_2^+ \Sigma - O_2^+ \Pi$ (500-600 nm).[21] This latter band system has the potential for quantitative molecular oxygen concentration measurements, but is limited by an excitation cross-section[10] of 10^{-21} cm^2, which is two orders of magnitude lower than the first negative system of N_2^+. Extensive laboratory study of this system is required before a quantitative molecular oxygen density measurement technique can be evaluated. Although both molecular oxygen and nitrogen can be induced to fluoresce with laser sources (O_2 with 193-nm excitation from an argon-fluoride laser[22] and N_2 with two-photon excitation[23] at 143 nm), neither technique is currently well developed for quantitative applications. In addition, the miniaturization of appropriate laser sources for flight research is as yet an undeveloped technology.

Measurement of minor species concentrations is important for understanding the role of nonequilibrium temperature and chemistry in transatmospheric flight. The high-temperature, nonequilibrium shock layer at the nose of a hypersonic vehicle will produce the minor species O, N, and NO. In the hypersonic boundary layer around the vehicle, the concentration of these species would be expected to be sensitive to the temperature and density distribution through the shock layer.

Electron-beam fluorescence of O atoms and N atoms has not been studied as a quantitative method for density measurement in gas dynamics. In the presence of molecular oxygen, determining O-atom concentration is difficult because of the interference of O^+ and O^{++} produced from electron-beam excitation of O_2. Differentiation of the parent atom or molecule may be possible from differences in the details of the excitation process, which could produce variation in the line structure and intensity. The soundness of this approach, however, has not been demonstrated and will require extensive laboratory investigation. Nitric oxide (NO) has been studied with electron-beam fluorescence.[20] The observed spectrum was identified as the $A^2\Sigma - X^2\Pi$ transition, with a band structure from 230 to 268 nm. Quantitative density measurements are complicated by self-absorption and therefore have not been developed for gas dynamics applications. Because of its expected appearance in the electron-beam fluorescence spectrum produced in a hypersonic boundary layer, a detailed laboratory study of the excitation-emission process will be essential.

Laser-induced fluorescence of the minor species found in a high temperature hypersonic boundary layer has been demonstrated in laboratory research. O-atom[24] and N-atom[24] LIF require two-photon excitation processes that are feasible in the laboratory but are too complex for flight research without powerful miniature laser sources. The NO molecule is the most likely candidate to be measured in flight using single-photon laser-induced fluorescence excitation. In combustion research, nitric oxide concentration measurements have been made[25] in flames at number densities of 10^{14} cm^{-3} and temperatures around 2000 K with LIF. At or below room temperature, one- and two-photon LIF of NO has been used in wind tunnel applications.[26]

At high temperature, the NO fluorescence spectrum becomes complex as more rotational and vibrational levels in the molecule are populated. The rotational line positions and line strengths can be calculated[27] for various electronic transitions in NO and can be compared with spectroscopic observations.[28] An example of the complexity of the NO

spectrum and its dependence on temperature is illustrated in Fig. 7.0.9. The rotational structure of fluorescence excitation spectra for the (0,0) vibrational band of the $A^2\Sigma - X^2\Pi$ transition at 226.2 nm was calculated[27] as a function of gas temperature from 300 to 2400 K. For this electronic transition, 12 branches are allowed that follow quantum mechanical selection rules for rotational-state change. In terms of the the rotational quantum number N (N equals the total angular momentum quantum number apart from electronic spin), six main-branch transitions (R_1, Q_1, P_1, R_2, Q_2, P_2), four primary satellite transitions (R_{21}, Q_{21}, Q_{12}, P_{12}), and two secondary satellite transitions (O_{12}, S_{21}) are present. In general, the main-branch transitions and primary satellite transitions directly overlap, since they differ only in the spin state of the $A^2\Sigma$ level, which has negligible energy difference. In Fig. 7.0.9a, the relative fluorescence signal levels for the R, P, and Q branches, along with the overlapping primary satellites, are plotted individually and combined for a gas temperature of 300 K. The relative fluorescence signal has been normalized by the strongest feature at 300 K, the Q_1+Q_{21} (N=10) transition. The combined spectrum in Fig. 7.0.9a covers 2 nm and displays the high density of states, with the R_1 and Q_1 features the most prominent. At 600 K this rotational structure still has identifiable peaks (Fig. 7.0.9b), while at 1200 K a significant broadening and reduction in signal level over of the entire band has taken place (Fig. 7.0.9c). At 2400 K the broadened vibrational band extends over 4 nm as more than 100 rotational levels are thermally populated (Fig. 7.0.9d).

At high concentration the (0,0) band is difficult to use for quantitative NO density measurements because of self-absorption of the fluorescence. Although the (1,0) band at 215 nm has a factor-of-two higher vibrational-band oscillator strength,[28] selecting weaker transitions in this band with subsequent fluorescence in the (1,1) band at 224 nm provides a measurement scheme without severe absorption effects. The rotational structure of the fluorescence signal should be similar to that given in Fig. 7.0.9. In either scheme, modeling of the excitation/fluorescence process will be necessary to design an optimal detection system. The effects of both quenching and rotational/vibrational energy transfer must be included if measurements at high density are to be made.

In laboratory experiments, comparison of LIF measurements of nitric oxide along with electron-beam fluorescence experiments should prove useful in the quantitative interpretation of spectra. Flight research using LIF of the NO molecule will require the development of a miniature tunable uv laser.

Program Plan for Developing Advanced Optical Diagnostics

In the preceding discussions, recommendations on the feasibility of using advanced optical diagnostic techniques for hypersonic flight research were presented. Electron-beam and laser-induced fluorescence techniques were identified as the most promising spectroscopic methods for use in flight experiments on the SWERVE Hypersonic Research Vehicle (SHRV). Electron-beam fluorescence spectroscopy is the most developed and is therefore best suited for immediate development for flight research. Although a method based on a combination of electron-beam and laser-induced techniques for in-flight velocity measurements has been identified, the general applicability of laser-induced fluorescence spectroscopy to flight research will require further development of miniature lasers. Recommendations on the development of miniature lasers are presented in the Flight Hardware Specifications Section. We present here an outline of a program plan to develop the diagnostic techniques that have been recommended above for flight research experiments.

Since the development and application of advanced optical diagnostics for hypersonic research has been dormant for the last dozen years, a program for resurrecting and modernizing electron-beam fluorescence techniques for flight research will necessarily require simultaneous efforts in laboratory research, wind tunnel experiments, and flight experiments on a vehicle such as SHRV. This multi-track program is described in the time line presented in Fig. 7.0.10, where each of these tasks is identified and sequenced such that it will support the next level of application.

Laboratory Research: To modernize electron-beam fluorescence spectroscopy, laboratory research is necessary to introduce the latest detector technology and signal processing methods into the technique. Spectroscopic codes for extracting pertinent gas properties need validation for the specific conditions to be encountered in hypersonic flight. Data analysis schemes that can efficiently minimize signal acquisition time and data structure size, and that can take advantage of unique on-board computational capabilities of imaging detectors, need evaluation. In the time line for the laboratory research program, two years has been allocated for electron-beam diagnostic evaluation. The spectroscopic codes developed during this period can then be used to interpret ground test data obtained in wind tunnels and flight experiments. Since it is expected that improved miniature laser sources will be available in the near future, we propose a subsequent period of two years for development of laser and combined laser/electron-beam techniques. New diagnostic

22

methods developed during this period can be incorporated into the redesign and modification of ground test instrument packages and future flight experiments. Computer codes for modeling and analysis of these new spectroscopic techniques will continue to need laboratory development for subsequent application to wind tunnel and flight experiments.

Wind Tunnel Experiments: The design of an optical diagnostic package for hypersonic flight research can be initiated at the same time as the laboratory studies. The conceptual design of this instrument has been identified in the course of this feasibility study. Two years have been set aside in the program time line for engineering, assembly, and test of the first instrument package (Unit #1) to be installed in a full-scale model of SHRV. Evaluation of the instrument package should be performed in a ground test program with experiments in the Mach 10 wind tunnel at AEDC and the Mach 18 shock tunnel at CALSPAN (Buffalo, NY). These facilities are desirable because they already have or will soon have electron-beam diagnostic capabilities that can define the wind tunnel flow-field conditions. This ground test program will provide a necessary bench mark early in the flight research program to validate the instrument design and the spectroscopic codes for data analysis. An additional benefit will be the hypersonic boundary-layer measurements obtained in the wind tunnel experiments. Since a version of SHRV has previously flown in these tunnels, the addition of flow-field measurements from the optical diagnostic experiments to previous aerodynamic and heat transfer data will provide a more complete data base for validation of computational fluid dynamic (CFD) codes. This comparison of SHRV flow-field data with CFD predictions prior to the flight experiments will be very useful in establishing a close working relationship between the experimental and computational project teams. This interaction will assure that the CFD codes can effectively utilize flight research data and will allow expeditious refinement of recommendations for flight profiles that yield optimal CFD validation. After these initial ground test experiments, the instrument package installed in the wind tunnel test model can be modified to evaluate new optical diagnostic techniques developed in the laboratory research. Continued evaluation of these techniques in further wind tunnel experiments will lay the foundation for their incorporation into future hypersonic flight research efforts.

Flight Research: The flight research experiments will build upon the laboratory studies for the development of the spectroscopic diagnostic techniques and the ground test program to validate the design of the flight instrument. The major hardware engineering task for the flight research instrument package (Unit #2) is development of a system that meets the

requirements of the SHRV specifications. On-board electrical power, detector cooling, cryro-pumping, and data-handling hardware will be needed. Two years have been assigned for the engineering, assembly, and testing of the flight research instrument package. An additional year is reserved for the testing and evaluation of telemetry schemes and data analysis. The current flight research plan designates the first two SHRV flights for moderate Mach number (<15) and moderate altitude (<50 km) to examine issues related to turbulent boundary layers, aerodynamic heating, control surfaces, etc. On the second of these flights, the optical diagnostic package should be flown for component and system evaluation. Although the primary flight objective will be boundary-layer and other aerodynamics experiments, the flight research instrument package should also be tested for operational capability. The optical diagnostic flight experiments could be scheduled for the third and fourth flights, respectively. It is possible that new experimental methods developed in the laboratory and applied in the wind tunnel ground tests can be included in subsequent flights.

References

1. F. G. Blottner, "Viscous Shock Layer at the Stagnation Point with Nonequilibrium Air Chemistry," AIAA J. **7**, 2281 (1969).

2. R. F. Bergeron and A. E. Kaplan, "Ballistic Missile Defense Advanced Development Program," Bell Telephone Laboratories Reentry Physics Studies Report (RPSR 71-12), September 1971.

3. V. Cuda and J. Moss, "Direct Simulation of Hypersonic Flows over Blunt Slender Bodies," AIAA Paper 86-1348, Fourth AIAA/ASME Joint Thermophysics Conference, Huntsville, AL, June 1986.

4. W. B. Kunkel and L. Talbot, "Ion Tracer Technique For Airspeed Measurement at Low Density," NACA Technical Note 3177, March 1954.

5. K. A. Butefisch, "Absolute Velocity Determination in a Hypersonic Low Density Flow," AIAA J. **9**, 1639 (1971).

6. K. A. Butefisch and D. Vennemann, "Absolute Velocity Measurements in a Rarefied Gas Flow by an Ion Time-of-Flight Technique," in *Rarefied Gas Dynamics* (Academic Press, New York, 1974), pp. 245-252.

7. G. Dupeyrat and M. Giat, "Experimental Study of Velocities in a Free Jet in a Rarefied Atmosphere," AIAA J. **14**, 1706 (1976).

8. E. E. Ferguson, "Measurements of Ionosphere Ion-Molecule Reactions Rates," Rev. Geophys. Space Phys. **12**, 703 (1974).

9. M. Mitchner and C. H. Kruger, *Partially Ionized Gases* (John Wiley & Sons, New York, 1973).

10. E. P. Muntz, "The Electron Beam Fluorescence Technique," AGARDograph, Vol. 132, December 1968.

11. R. J. Cattolica, F. Robben, L. Talbot, and D. R. Willis, Phys. Fluids **17**, 1743 (1979).

12. M. Becker, F. Robben, and R. J. Cattolica, AIAA J. **12**, 1247 (1974).

13. R. J. Cattolica, R. Gallager, J. B. Anderson, and L. Talbot, AIAA J. **17**, 344 (1979).

14. B. N. Sraivastava and I. M. Mirza, Phys. Rev. **168**, 86 (1986).

15. E. P. Muntz, Phys. Fluids **20**, 80 (1962).

16. R. W. Nicholls, Amer. Geophys. **20**, 819 (1967).

17. L. V. Wallace and R. W. Nicholls, J. Atmos. Terr. Phys. **7**, 101 (1955).

18. D. Coe, R. Robben, R. J. Cattolica, and L. Talbot, Phys. Fluids **23**, 706 (1980).

19. P. F. W. Gribbon and D. T. Stewart, *The Airglow and the Aurora* (Pergamon, New York, 1955).

20. E. P. Muntz and D. J. Marsden, *Rarefied Gas Dynamics*, Vol. II, p. 495, 1963.

21. D. T. Stewart and E. Gabthuler, Proc. Phys. Soc. **72**, 287 (1958).

22. K. Shibuya and F. Stuhl, J. Chem. Phys. **76**, 1184 (1982).

23. H. Helvajain, B. M. Dekoven, and A. P. Baronavksi, J. Chem. Phys. **90**, 175 (1984).

24. W. K. Bischel, B. E. Perry, and D. R. Crosley, Appl. Opt. **21**, 1419 (1981).

25. C. Morley, in *Eighteenth Symposium on (International) on Combustion* (Combustion Institute, Pittsburgh, 1981), pp. 23-32.

26. K. P. Gross and R. L. McKenzie, AIAA J. **23**, 1932 (1985).

27. I. Kovacs, in *Rotational Structure in the Spectra of Diatomic Molecules* (Elsevier, New York, 1969).

28. R. Engleman Jr., P. E. Rouse, H. M. Peek, V. D. Baiamonte, Los Alamos Scientific Laboratory Report, LA-4364, UC-34, Physics, TID-4500, July 1970.

Table 7.0.1. Boundary-layer properties for an 8° sphere-cone body at a stream-wise location 332 cm from the nose.

Mach Number: 21

Altitude: 55 km

Boundary-Layer Thickness: 20 mm

Density (minimum): $5.0 \cdot 10^{-8}$ gm/cm^3
                     $1.0 \cdot 10^{15}$ cm^{-3}

Velocity: 6.8 km/s

Temperature: 4400 K

Major Species: N_2 $7.8 \cdot 10^{14}$ cm^{-3}
                O_2 $1.8 \cdot 10^{14}$ cm^{-3}

Minor Species: NO $1.0 \cdot 10^{12}$ cm^{-3}
                O $1.0 \cdot 10^{12}$ cm^{-3}
                N $1.0 \cdot 10^{12}$ cm^{-3}

Table 7.0.2. Prominent vibrational bands in the electron-beam-excited fluorescence spectrum of the $B^2\Sigma(v') - X^2\Sigma(v'')$ transitions in the N_2^+ ion.

v',v"	wavelength (nm)	radiative lifetime (ns)
0,0	391.4	66
0,1	427.8	66
1,0	358.2	94
2,1	356.3	116
3,2	354.8	164

HIGH TEMPERATURE (3000 K) - HIGH PRESSURE (100 atm)

FREE JET SOURCE
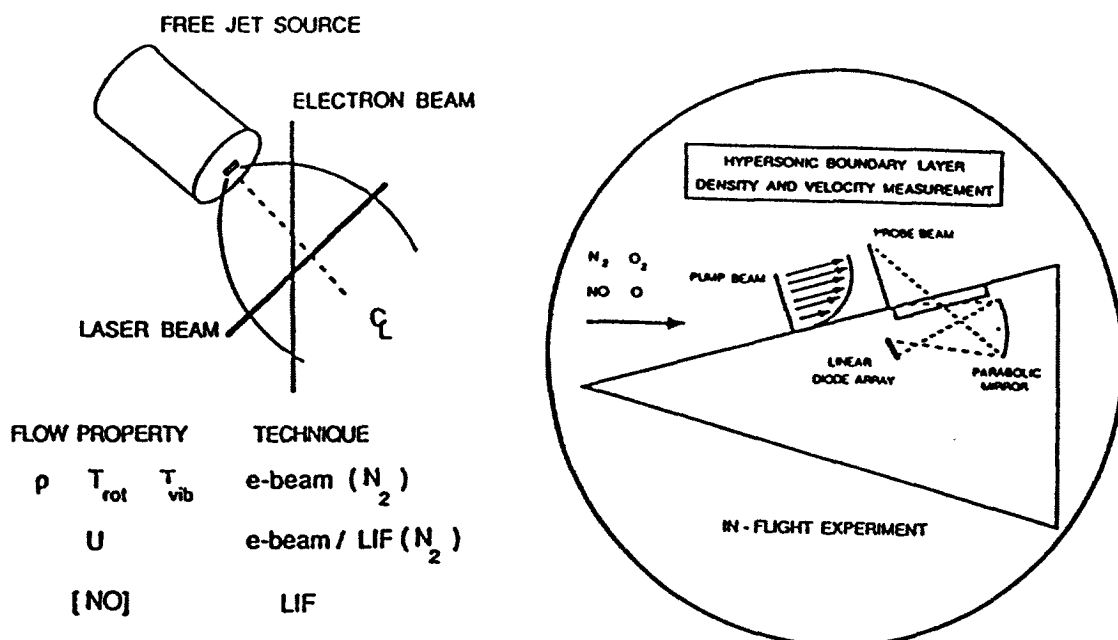
Figure 7.0.1. Laboratory hypersonic free-jet and in-flight experiments.
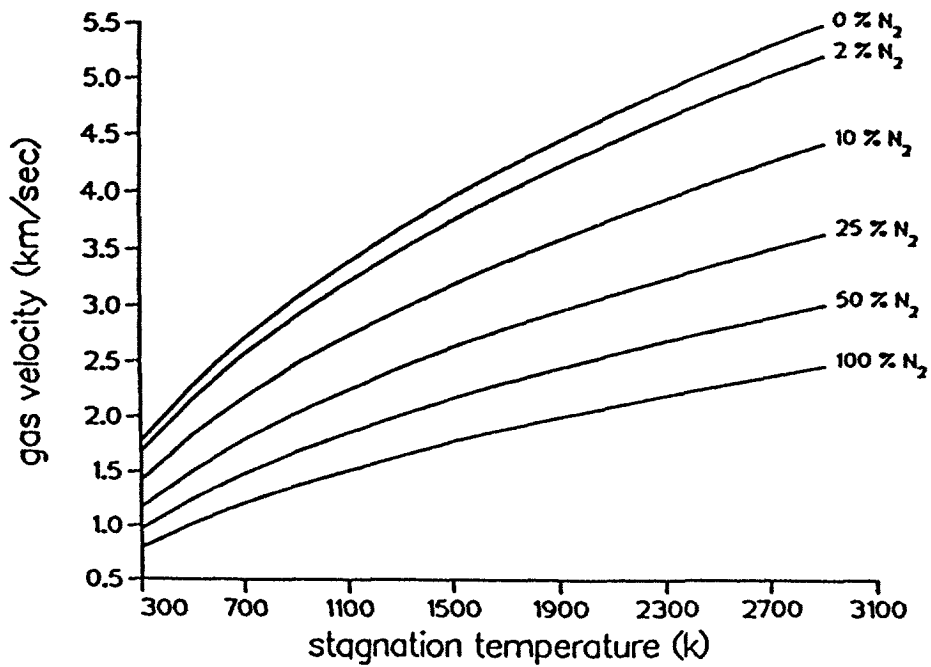

Figure 7.0.2. Limiting velocity of He/N_2 mixture in hypersonic free-jet experiment.
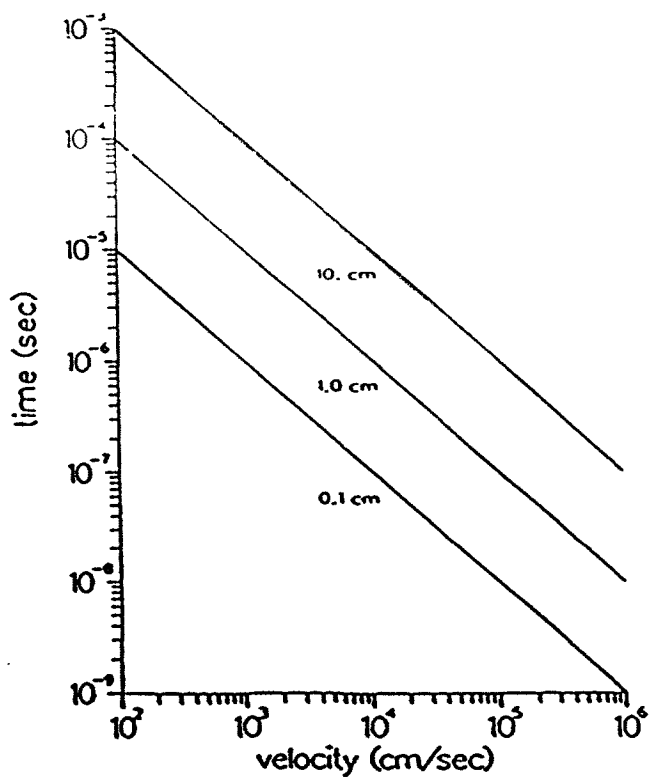
Figure 7.0.3. Required temporal resolution for time-of-flight velocity measurement with 1% accuracy. Flight path length is indicated in centimeters.
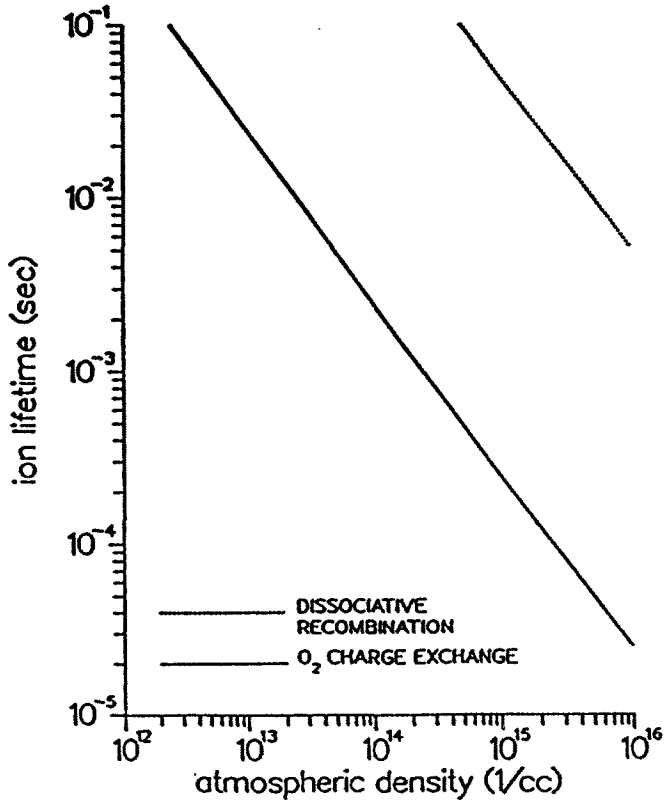

Figure 7.0.4. N_2^+ lifetime for dissociative recombination and charge exchange with O_2.

29
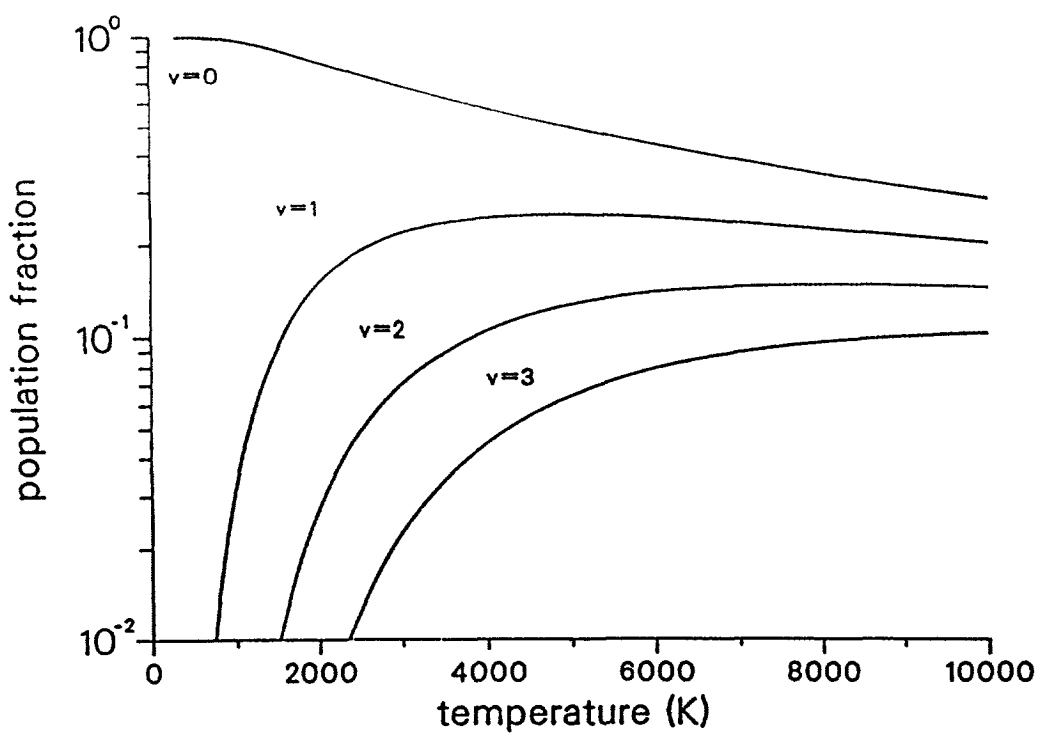
Figure 7.0.5. Vibrational-population distribution in N_2 as a function of temperature.
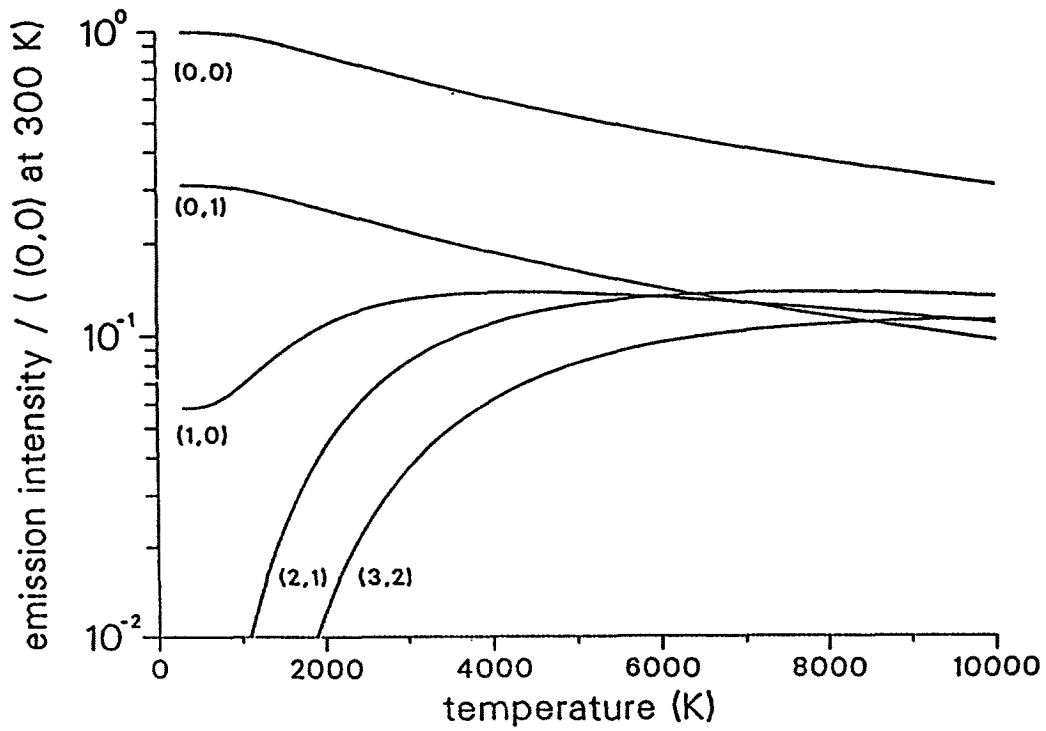
Figure 7.0.6. N_2^+ vibrational-band emission strength as a function of temperature.

30
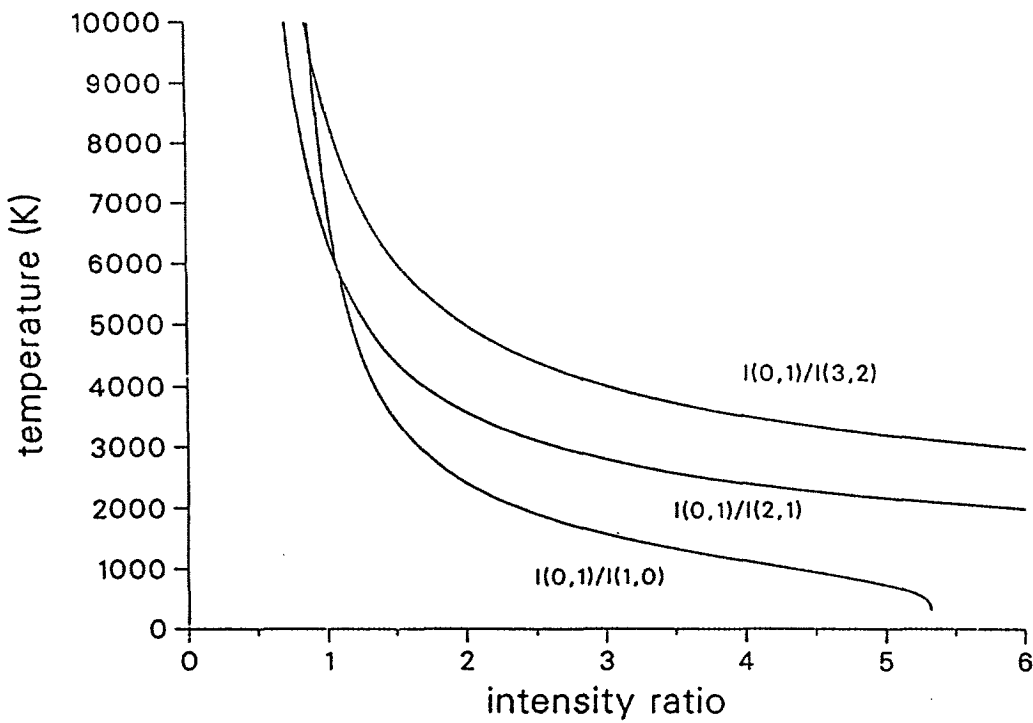
Figure 7.0.7. Ratios of N_2^+ vibrational-band signal strength as a function of temperature.
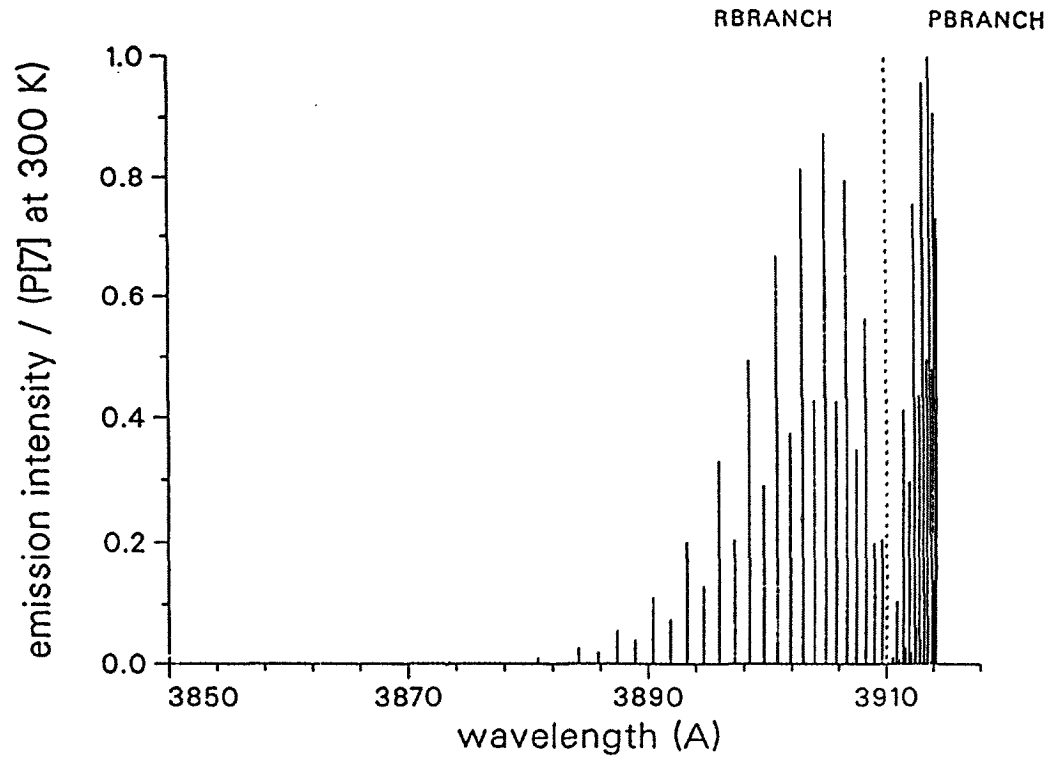
Figure 7.0.8a. Rotational spectrum in the (0,0) band of the $B^2\Sigma$ to $X^2\Sigma$ transition of the
N_2^+ ion at 300 K.
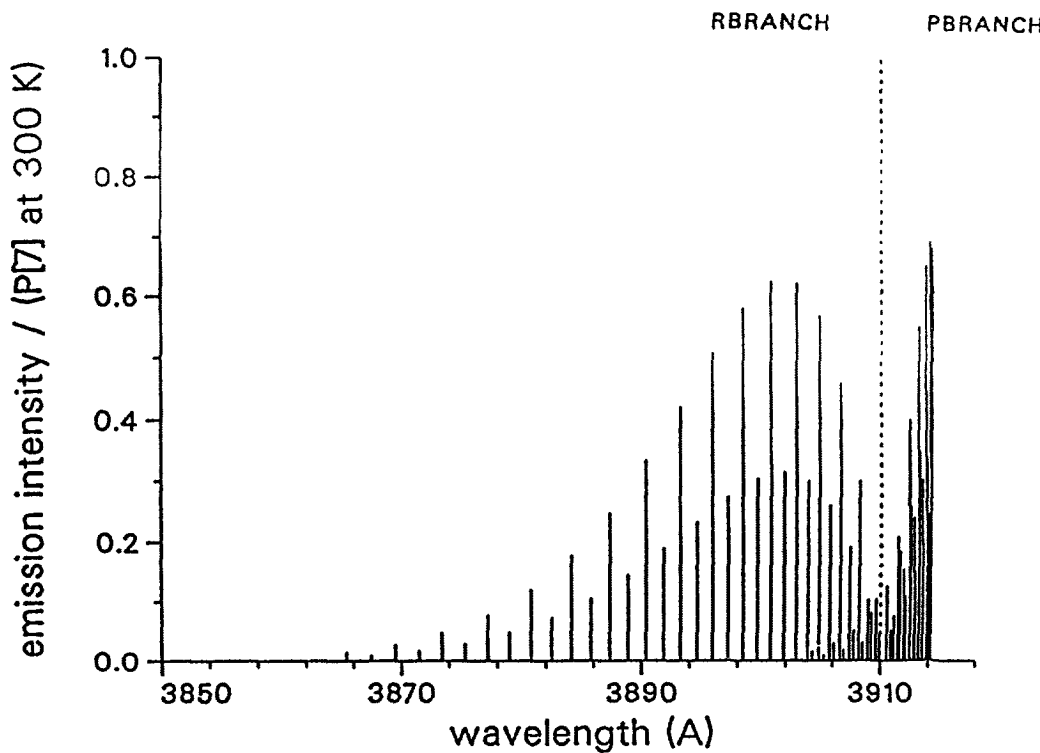
Figure 7.0.8b. Rotational spectrum in the (0,0) band of the $B^2\Sigma$ to $X^2\Sigma$ transition of the N_2^+ ion at 600 K.
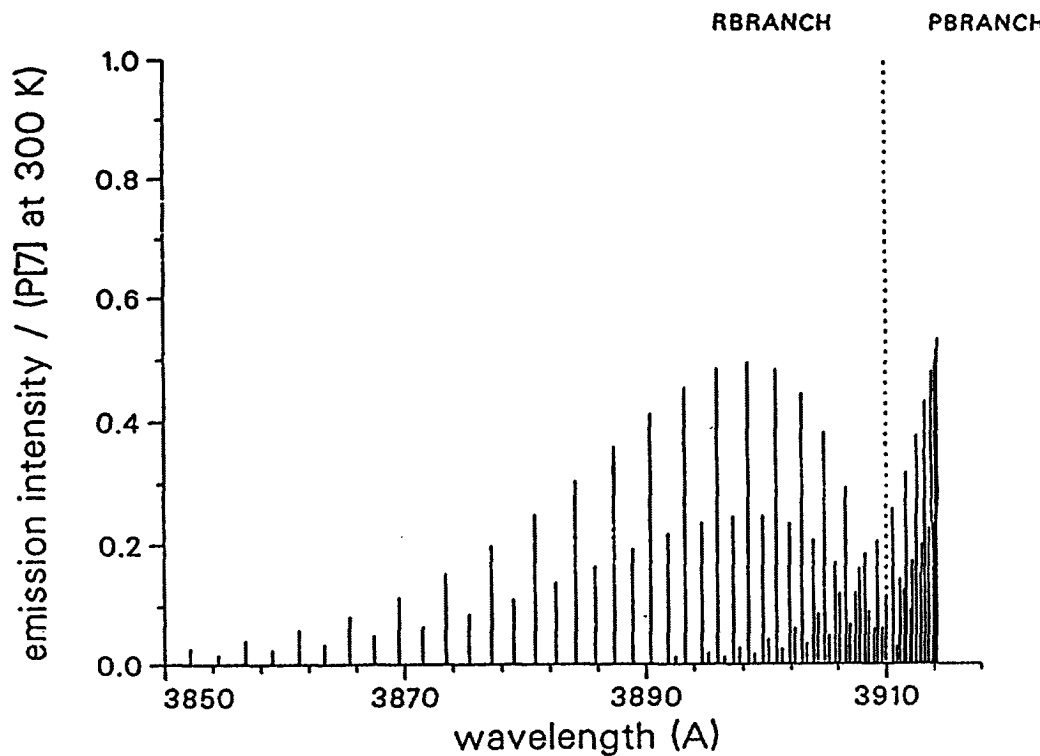
Figure 7.0.8c. Rotational spectrum in the (0,0) band of the $B^2\Sigma$ to $X^2\Sigma$ transition of the N_2^+ ion at 1000 K.
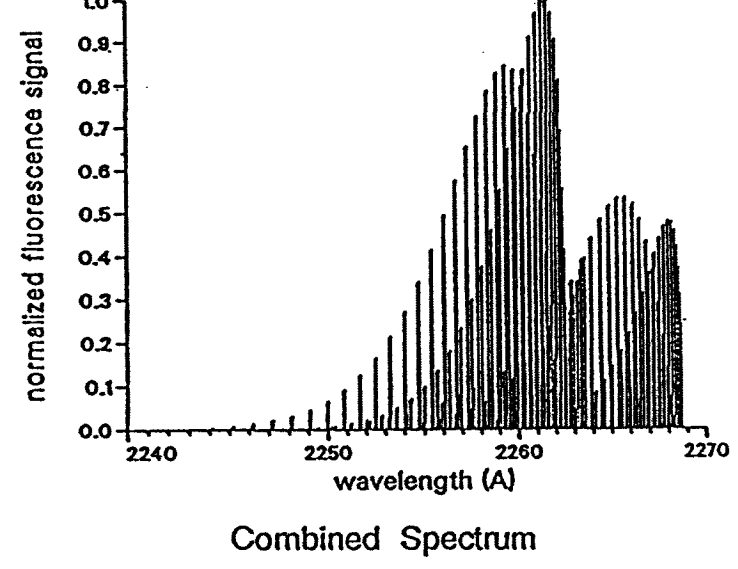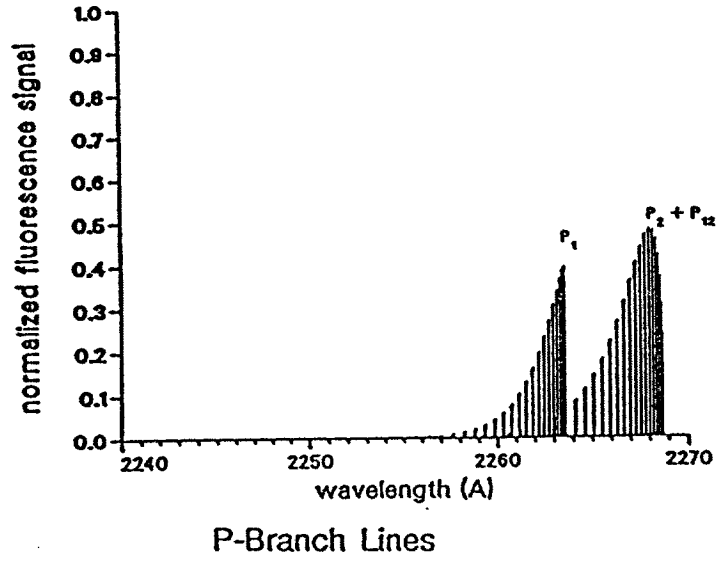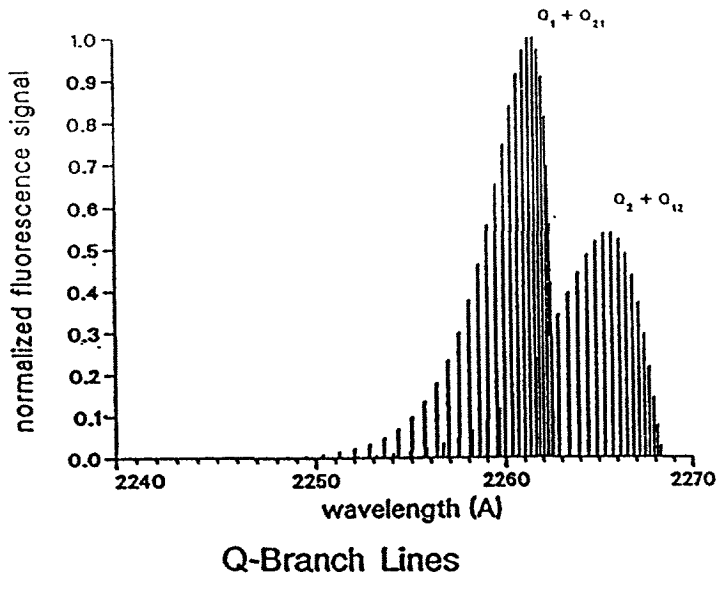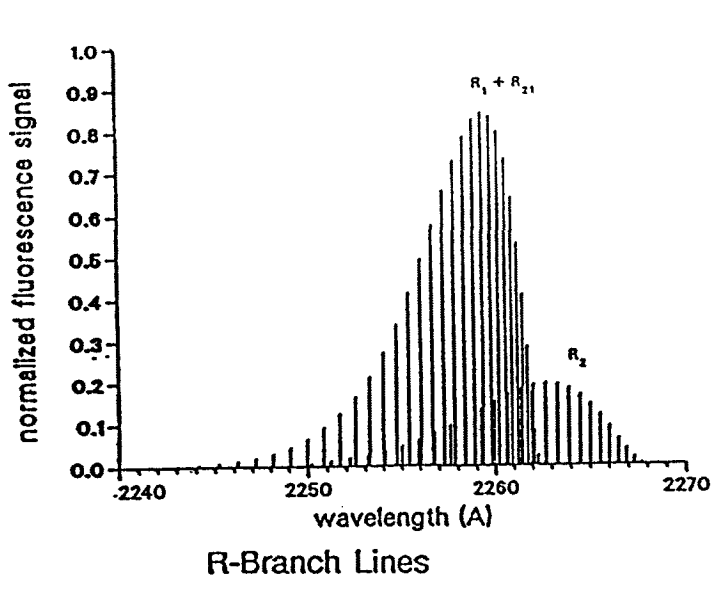
Figure 7.0.9a. Fluorescence excitation spectra for the (0,0) band of the $A^2\Sigma - X^2\Pi$ transition of NO at 300 K.

33
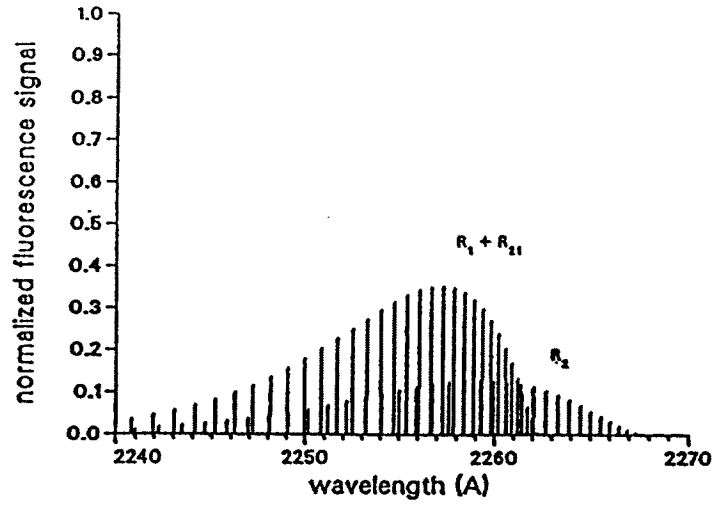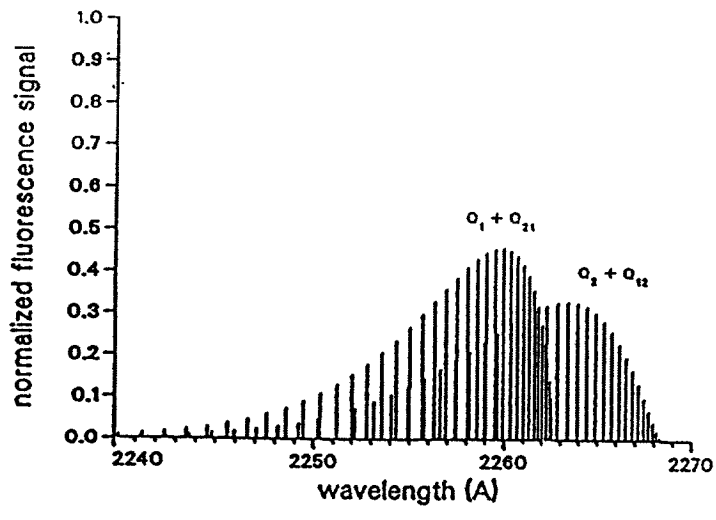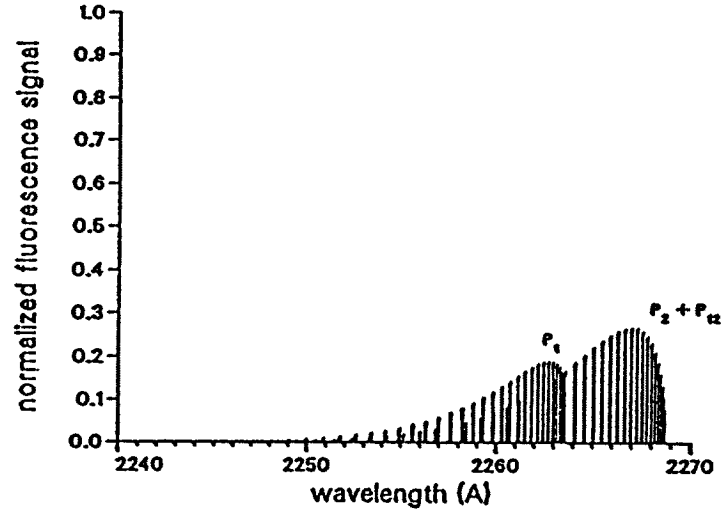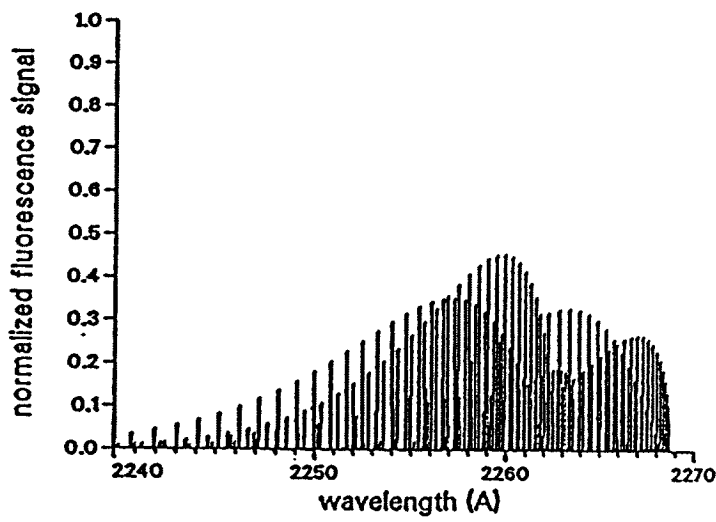
Figure 7.0.9b. Fluorescence excitation spectra for the (0,0) band of the $A^2\Sigma - X^2\Pi$ transition of NO at 600 K.
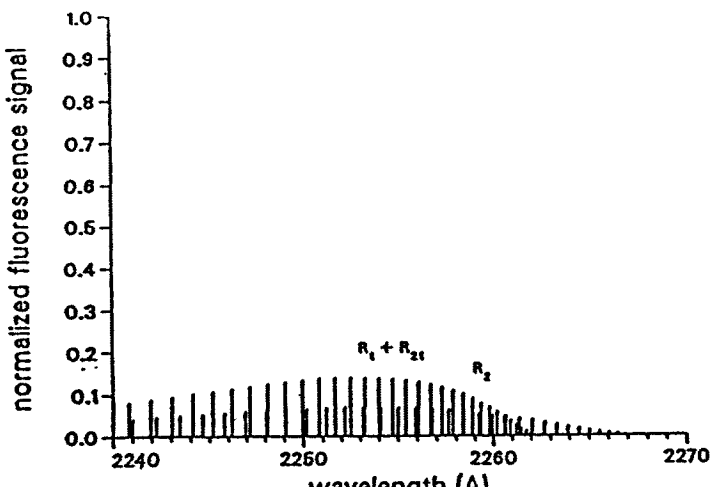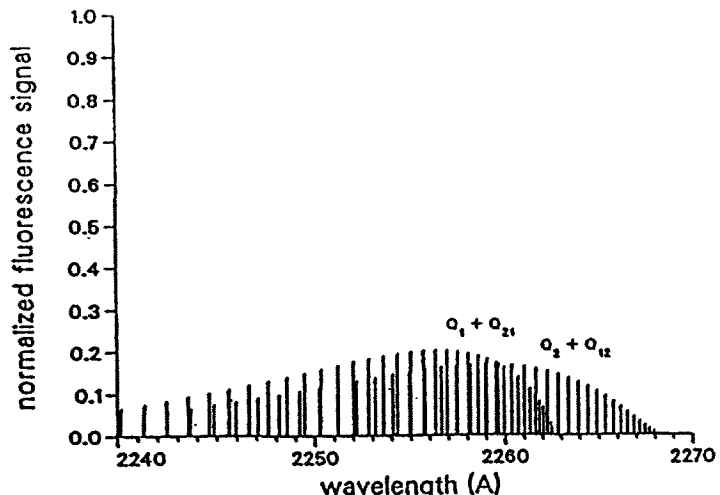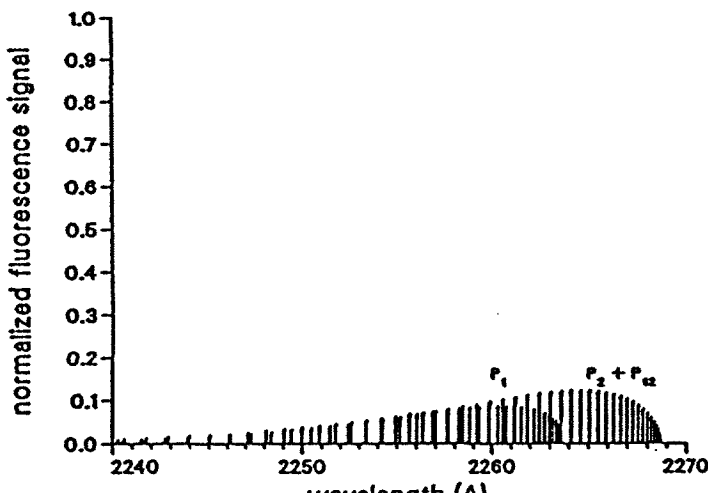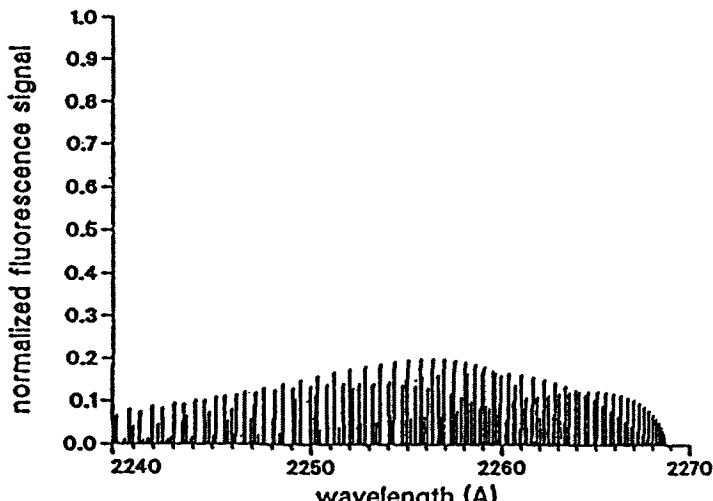
Figure 7.0.9c. Fluorescence excitation spectra for the (0,0) band of the $A^2\Sigma - X^2\Pi$ transition of NO at 1200 K.
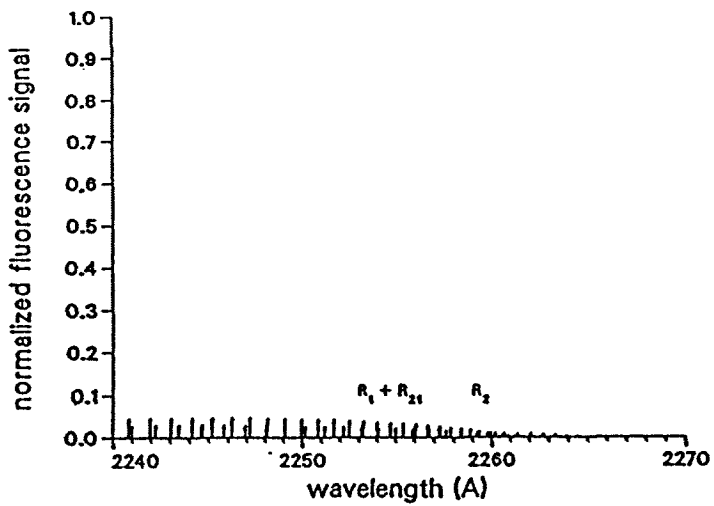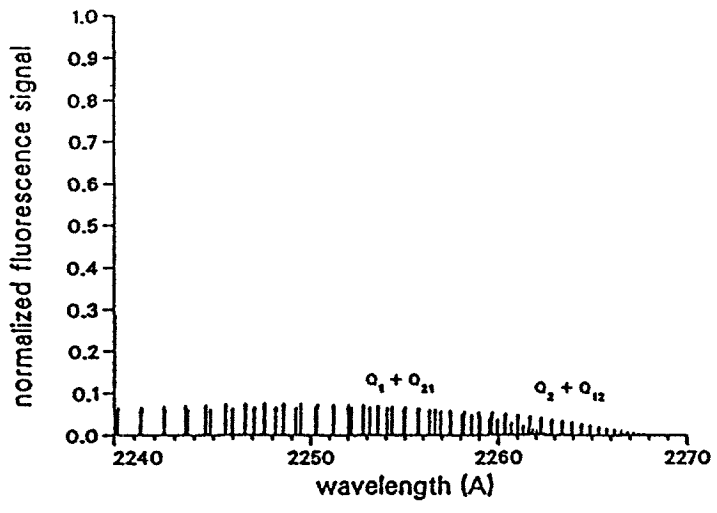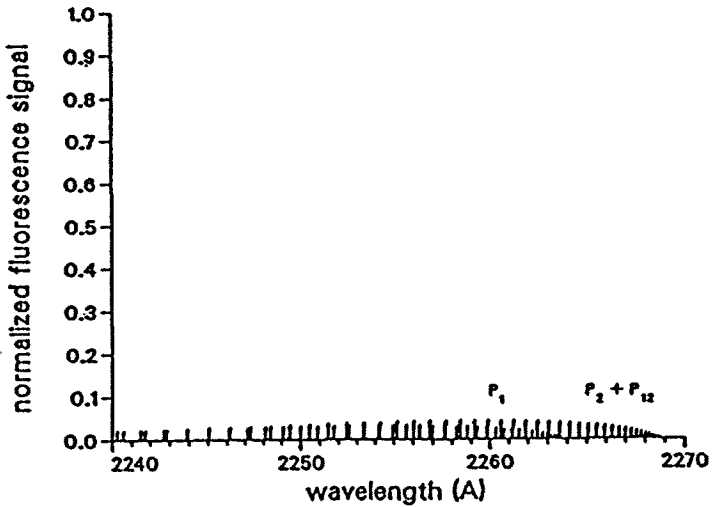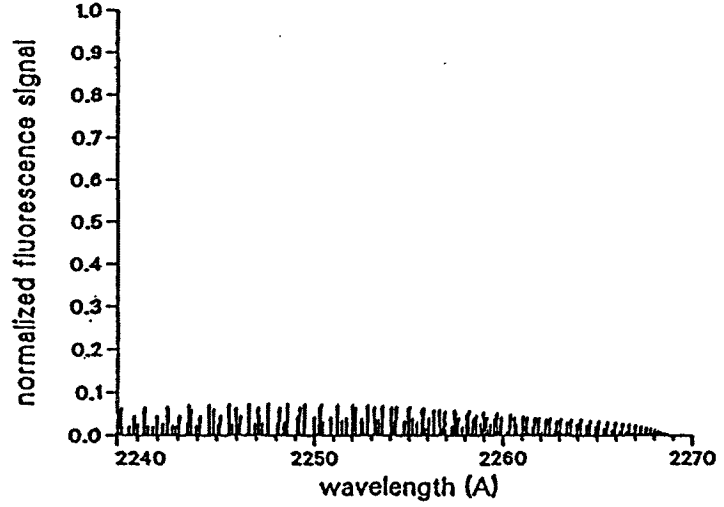
Figure 7.0.9d. Fluorescence excitation spectra for the (0,0) band of the $A^2\Sigma - X^2\Pi$ transition of NO at 2400 K.

36

	FY 88	FY 89	FY 90	FY 91	FY 92	FY 93	FY 94	FY 95

Laboratory Research:

Electron Beam Diagnostics	New E-beam and Laser Techs.	Diagnostic Development

(Spec. Code)   (new optical techniques)   (Spec. Code)

Wind Tunnel Experiments Unit # 1

Engineering	Assembly & Test	Mach 10 Tunnel Exp.	Mach 18 Tunnel Exp.	Modifications New Techs.	Assemby & Test	Wind Tunnel Experiment

(CFD Data)   (CFD Data)   (CFD Data)

Flight Research Experiments Unit # 2

Engineering Vehicle Integ.	Assembly & Test	Telemetry & Data Analysis	Component Flight Test	Flight Experiment	Flight Experiment

(CFD Data)   (CFD Data)

SHRV Flight Schedule   Flt. No. 1   Flt. No. 2   Flt. No. 3   Flt. No. 4

Figure 7.0.10.   Program plan for developing advanced optical diagnostics for SHRV flight research.

7.2 Flight Hardware Specifications

Introduction

In the Flight Experiment Study and Evaluation Section, several experiments to measure boundary layer properties around the SWERVE Hypersonic Research Vehicle (SHRV) were discussed. These experiments require hardware including laser and electron beam sources, and optical detection systems. In this section we discuss the specifications of this hardware, the availability of hardware that meets these specifications, and the feasibility of developing hardware which is not presently available. Electron beam sources have already been used in flight experiments with good success. These sources adequately meet the specifications required for the SHRV boundary layer experiments, and we do not discuss them further in this section. Miniature laser sources for flight experiments, on the other hand, are not readily available, even though their development is progressing rapidly. Thus, we begin with a discussion of laser sources that would be used for the experiments described in the Flight Experiment Study and Evaluation Section. Since these lasers require substantial power, we also discuss the capabilities of battery and power supplies for operating the lasers and other experimental hardware.

A discussion of the specifications for spectrograph instrumentation, including array detectors, follows the section on laser sources. Requirements for fused silica windows, estimations of electron-beam fluorescence signal levels, possible interference from spacecraft glow, and data acquisition considerations are also examined. Conclusions and recommendations complete this section.

Laser Sources

The ideal laser source for laser-induced fluorescence experiments in flight applications is an all solid-state laser system. Diode-laser-pumped solid-state lasers (Nd:YAG, YLF, NPP) and tunable solid-state lasers (Ti:Al_2O_3) are potential candidates, but these lasers are still in the developmental stage. Diode-laser-pumped intracavity frequency-doubled Nd:YAG lasers will be commercially available soon, but their applicability will be limited since their wavelength is fixed (532 nm).

Miniature sealed-plasma-tube N_2 lasers (337 nm) that may be suitable as probes for electron-beam-excited N_2^+ are commercially available (Laser Science, Inc.). These lasers,

38

which can deliver 100-μJ pulses at 20 Hz, measure 9 3/4" x 4 1/2" x 2 1/2" (including power supply), and can be operated from a 12-V battery. Miniature excimer lasers using sealed-plasma-tube technology are being developed at Los Alamos National Laboratory and elsewhere. These lasers may be used directly for the spectroscopy of NO if sufficient overlap between the excimer laser emission and an appropriate NO absorption band is achieved, either directly or by Raman shifting the laser wavelength. Frequency-doubled dye lasers can pump the NO γ(0,0) band, and it should be possible to develop flight-qualified dye laser systems. However, all of these laser systems need additional laboratory development before meeting in-flight requirements.

The sealed-tube nitrogen (N_2) laser shows the greatest promise for near-term use in the SHRV flight instrumentation. A miniature nitrogen laser could be used as the probe laser in velocity measurements by ion time-of-flight (described in the Flight Experiment Study and Evaluation Section). While the wavelength, pulse energy, and pulse length of commercially available nitrogen lasers meet the requirements for this experiment, some laboratory development will be required to optimize the nitrogen laser for the time-of flight experiments. The pulse timing jitter, for example, must be about 2 ns or less to allow on-chip data averaging and still preserve the accuracy of the velocity measurement.

A comparison of two commercially available nitrogen lasers is given in Table 7.2.1. The PRA laser has a short pulse length and low timing jitter that make it desirable for laboratory tests. Unfortunately, the PRA laser is too large for flight experiments and requires a gas flow system. The LSI laser is small enough for flight experiments and has a sealed, disposable plasma tube. But the long pulse length and timing jitter of the LSI laser must be improved before this laser can be used for flight experiments. Both of the lasers listed in Table 7.2.1 should be purchased for evaluation in laboratory bench tests.

Miniature N_2 lasers may be useful for several flight instrumentation applications. One application is to pump a dye laser tuned to absorptions in the (first negative system) $B^2\Sigma_u^+ - X^2\Sigma_g^+$ (0,0) band of N_2^+ (391.44 nm) for laser-induced fluorescence (LIF) time-of-flight velocity measurements. The feasibility of these measurements depends on the efficiency of the dye laser and the absorption cross-section for the transition. Another application would be to modify the laser to lase on N_2^+ (427.81 nm) to overlap directly the $B^2\Sigma_u^+ - X^2\Sigma_g^+$ (0,1) absorption band of N_2^+. This is a common option for large N_2 lasers, but a miniature laser may not have enough gain to lase on N_2^+. A third application,

if secondary electrons (~9 eV) create enough excited-state N_2 in the hypersonic boundary layer, is that the 337.1-nm laser beam could be used directly for LIF on the (second positive system) $C^3\Pi_u - B^3\Pi_u$ band of N_2. All of these applications will require laboratory development to demonstrate their feasibility for in-flight experiments.

We have been evaluating a commercial miniature nitrogen-laser-pumped dye laser[1] for use in flight experiments. The results of preliminary measurements are summarized in Table 7.2.2. The nitrogen laser produces 4-ns pulses at 337 nm. The output energy is 100 μJ/pulse at repetition rates of up to 20 Hz. The linewidth of the nitrogen laser is ~0.1 nm (1.0 Å). The pulse-to-pulse jitter of the nitrogen laser is ±50 ns.

While the output of the nitrogen laser is fixed at 337 nm, the dye laser is tunable over the range of 365 nm to 950 nm using a variety of dyes. Initial tests of the dye laser were performed using Coumarin 440 laser dye in ethanol. Although not yet optimized for output power or beam quality, the laser output was 8 μJ/pulse at 440 nm. We expect to get >20 μJ/pulse with optimized dye concentration and beam alignment. The linewidth of the dye laser is ~1 nm, and its pulse length is 4 ns.

Although the nitrogen laser and nitrogen-laser-pumped dye laser are the most likely near-term candidates for flight experiments, other laser systems may be viable candidates in the future. Miniature excimer lasers,[2,3] for example, may serve as pump sources for tunable dye lasers or may be used directly in some experiments. The XeCl laser operates at 308 nm and may be used to excite directly the (0,0) band of the $A - X$ transition of the OH radical. A list of excimer lasers and their output wavelengths is given in Table 7.2.3.

Recent progress in miniature solid-state lasers[4-6] indicates that more flight-worthy lasers may be developed in the near future. Miniature Q-switched diode-laser-pumped Nd:YAG lasers with output energies of 20 μJ/pulse at 1.06 μm and 5 μJ/pulse at 532 nm are now commercially available.[7] More powerful lasers will undoubtedly be produced in the future. Although these lasers are not broadly tunable, they may be useful for pumping miniature dye lasers, and, ultimately, for pumping miniature tunable solid-state lasers.

Battery and Power Supply Capabilities

The battery design personnel (Divs. 2522 and 2523) at Sandia have designed several electrochemical battery configurations that satisfy the anticipated SHRV power

requirement for the experimental package, estimated to be ~1 kW @ 100 V for 5 min. We have selected this requirement because the laser sources have not yet been well defined, and the final source may require substantial power. However, it is likely that the final design for the experimental package will require less power. The choices for delivering powers at the above levels are the Li(Si)/FeS$_2$ thermally activated battery, the reserve lithium thionyl chloride battery (RLTC), the active lithium thionyl chloride battery (ALTC), and the active lithium sulfur dioxide battery (LAMB). Although the RLTC and the ALTC batteries are the most efficient power batteries, thionyl chloride is toxic and very corrosive in the presence of moisture. In addition, both the RLTC and the ALTC batteries can explode violently when subjected to extended short-circuit, fire, heat, crush, or other abuse conditions. The thermally activated battery is a very reliable and rugged power source, but the heat generated by the battery can bring the case temperature up to 250°C. As a result, this battery would have to be well insulated, both to increase its efficiency and to isolate the optical system from excessive temperature gradients. Also, the thermal battery is slightly larger that the others, but still capable of fitting easily into the available space allowed for the experimental package (roughly two cu. ft. for the whole package).

Spectrograph Instrumentation

Very compact spectrographs suitable for the SHRV experiments can be designed using commercially available microchannel-plate image intensifiers and two-dimensional charge-coupled device (CCD) array detectors coupled by flexible fiber-optic bundles. As Broadfoot *et al* (Univ. of Arizona) demonstrated with the Voyager uv spectrograph, spectrographs using intensified-CCD (ICCD) technology have significant advantages over traditional scanning spectrometers. Since the entire spectrum is recorded in parallel, ICCD systems have a photometric advantage (i.e., detected photons/second) of more than two orders of magnitude over scanning systems covering the same spectral range. The two-dimensional format of CCD arrays permits good spectral and spatial resolution, and allows multiplexing of data from several gratings and/or imaging systems onto one array for common detection and signal processing. For example, the spectra from several gratings, each of which covers a separate spectral region, can be imaged onto one ICCD, thereby covering a very wide spectral range (~80 nm/grating) with good spectral resolution (~0.3 nm). The size, weight, and power consumption of ICCD spectrographs will meet the SHRV requirements.

Initial experiments to measure density and temperature profiles of the boundary layer could use an electron-beam fluorescence technique. This experiment, shown schematically in Fig. 7.2.1, uses a collimated electron beam to produce a column of excited gas molecules in the boundary layer. The fluorescence from this excited column of gas is collected by an optical system and analyzed using an imaging spectrograph coupled to a two-dimensional ICCD detector. This spectrograph forms an image of the electron beam along one dimension of the detector array, and disperses an emission spectrum along the other dimension of the array. Thus, the imaging spectrograph can both spectrally and spatially resolve the fluorescence generated by the electron beam.

Spatially resolved fluorescence spectra can be used to determine profiles of the density, rotational temperature, and vibrational temperature in the boundary layer. Density can be determined by measuring the total fluorescence intensity as a function of position through the boundary layer. The fluorescence signal from the N_2^+ ion, for example, is linearly dependent on its density for number densities up to 10^{16} cm^{-3}. At higher number densities, the relationship becomes nonlinear. The rotational temperature of N_2^+ can be determined by detailed spectral analysis of the $B^2\Sigma - X^2\Sigma$ (0,0) band at 391.4 nm. This measurement requires a spectrograph with a resolution of 0.01 nm over a range of 1 nm. The vibrational temperature of N_2^+ can be determined by measuring the ratio of the fluorescence intensity from the (0,0) band at 391.4 nm to the fluorescence intensity from the (0,1) band at 427.8 nm. This measurement requires a spectrograph with a range of ~40 nm. The resolution of the spectrograph is not critical for the vibrational temperature measurement, since the integrated intensity of each band is measured, not the detailed structure of each band.

Since the rotational and vibrational temperatures in the boundary layer are probably not equal, both temperatures should be measured simultaneously. An imaging spectrograph with two gratings, one for rotational spectra and one for vibrational spectra, could be designed for this measurement. The basic layout of this spectrograph is shown in Fig. 7.2.2. One grating has the spectral resolution required for rotational temperature measurements. The second grating has the wide spectral range necessary for vibrational temperature measurements. The two gratings are tilted with respect to one another so that the imaged spectra (rotational and vibrational) are separated on the face of the ICCD sensor, as shown in Fig. 7.2.3.

The optical design of the dual-grating spectrograph is constrained by the sizes of the ICCD array and the electron-beam-excited column, and by the required spectral resolution. The CCD array dimensions and image format are shown in Fig. 7.2.3. In order to obtain the 1-part-in-100 resolution necessary for the rotational temperature measurements, the image of the spectrometer slit on the array must be 0.125 mm wide. Since the size of the fluorescing column is ~1 mm, the spectrograph must have a magnification of about 1/8.

The choice of the diffraction gratings and the camera lens (or mirror) focal lengths depends on the dispersion required in the image plane. The rotational temperature measurements require a dispersion of 0.08 nm/mm, while the vibrational temperature measurements require a dispersion of 3.2 nm/mm.

The linear dispersion in the focal plane of the spectrograph camera mirror (or lens) is given by:

$$\frac{d\lambda}{dx} = \frac{d\ \cos\theta}{mf}, \tag{7.2.1}$$

where f is the focal length of the camera lens or mirror, m is the diffraction order used, d is the groove spacing of the grating, and θ is the diffraction angle. The diffraction angle θ is constrained by the physical layout of the spectrograph and should be as small as practical. For the dual-grating spectrograph (Fig. 7.2.2), θ = 30 degrees. To minimize the size of the spectrograph, the focal length of the camera should be short. (At constant f/#, the volume of the spectrograph is proportional to the cube of the camera focal length.) Several choices for camera focal length, grating groove density, and diffraction order are listed in Table 7.2.4. Low-groove-density gratings (1200 g/mm) used in first order provide enough dispersion for the vibrational spectra, even when used with short focal length camera lenses. Unfortunately, high-groove-density gratings (6000 g/mm) must be used in higher orders to obtain enough dispersion for the measurement of rotational temperature.

An imaging spectrograph can be designed and built to measure the the density, rotational temperature and vibrational temperature of N_2^+. Prototypes of the spectrograph can be built with off-the-shelf mirrors, lenses and diffraction gratings, but the final instrument must be custom-designed and will require custom-built optics. Physically, the spectrograph should be designed as a solid-state instrument with no moving parts. The gratings, mirrors and lenses can all be made from fused silica. These parts can be carefully

aligned and permanently bonded to a fused silica "optical bench." The ICCD sensor should be detachable to allow several instruments to share the same detector/ electronics system.

A commercial CCD camera system, manufactured by Photometrics, Ltd., seems well suited for both laboratory feasibility studies and, with modest modifications, for use in flight experiments. All of the important operating parameters (such as readout format, on-chip summation, and preamplifier gain) are fully software programmable and can be reconfigured during the course of a flight experiment, if necessary. The electronic hardware is modular, and can be repackaged to meet the space requirements of the flight vehicle. In addition, this module will sample and digitize the CCD output, and store the spectra before the data is transmitted to the ground. Since both the camera control computer and the SANDAC flight-control computer are based on the Motorola 68000, we may be able to use already developed hardware and software in a special SANDAC module to control the CCD camera.

The technical specifications of the Photometrics camera system are summarized in Table 7.2.5. The camera system uses a Thompson CCD array with 384 (horizontal) by 576 (vertical) pixels. The pixel size is 23 μm by 23 μm. Other CCD arrays are available for the camera system. A three-stage thermoelectric cooler cools the CCD array to -50°C to reduce dark noise. At this temperature, the dark noise for our array is ~8.3 electrons/second. The quantum efficiency of the CCD is ~5% at 400 nm and ~30% at 500 nm.

We have interfaced the two-dimensional CCD camera to a miniature spectrograph to make a compact imaging spectrograph. The imaging spectrograph, illustrated in Fig. 7.2.4, is a simple instrument with only one optical element and no moving parts. An aberration-corrected, flat-field concave holographic grating provides both the spectral dispersion and the focusing required for the instrument.[8-10] This grating provides a flat-field spectrum over a 25-mm field of view. The CCD array detector is positioned in this focal plane. The specifications for the spectrograph[11] and a list of the gratings and slits are given in Table 7.2.6. Each grating has a focal length of 200 mm and operates at f/3. The overall length of the instrument is ~28 cm, including the CCD array housing. For flight experiments, both the concave grating and the CCD array could be repackaged to minimize the size and weight of the instrument. In addition, mirrors could be used to fold the optical path to make the instrument more compact.

44

The performance specifications of the imaging spectrograph are summarized in Table 7.2.7. For each of the gratings, Table 7.2.7 shows the spectral dispersion of the grating, the resolution of the system using that grating with a 50-μm entrance slit, the spectral range observable using the Thompson CCD array, and the spectral range that each grating is designed to cover. The highest resolution attainable with this system is 0.2 nm using the 1200-g/mm grating. The largest spectral range the instrument can cover is limited by the horizontal dimension of the array (8.3 mm) to 212 nm using the 200-g/mm grating. Custom concave holographic gratings are also available[12] for applications that require special focal lengths and groove densities.

Fused Silica Windows

The transparency and optical quality of the fused silica window of SHRV is critical to the success of the in-flight optical measurements. At room temperature, fused silica is transparent from ~190 nm to ~2 μm. At elevated temperatures, both the uv absorption edge and the ir absorption edge move closer together,[13-15] narrowing the spectral region of transparency. Fortunately, fused silica is transparent in the spectral regions of interest for the SHRV experiments (380 nm to 400 nm for N_2^+) for temperatures up to at least 1500°C (the maximum range tested). However, the uv absorption edge is near 240 to 250 nm at 1500°C, and could be a potential problem for observation of NO fluorescence spectra.

The design of the imaging spectrograph (or any other imaging instrument) must compensate for the thickness of the fused silica window to reduce optical aberrations to acceptable levels. Index-of-refraction gradients due to temperature gradients in the fused silica window will add complexity to the design of the optical system. In order to predict the performance of the imaging system, the temperature gradients on the surface and through the thickness of the fused silica window must be predicted. Optical ray tracing programs can then calculate the effect of these gradients on the quality of the image. Using this information, the optical designer can probably compensate for these gradients in the optical design (if the gradients are more or less constant throughout the flight profile). In addition, index-of-refraction gradients due to density gradients in the air surrounding the vehicle will affect the performance of the optical imaging system. As a result, measurements can be best made for laminar boundary layers since turbulence in the boundary layer will cause the image of the electron beam to move randomly, blurring the image over the time of the exposure.

Estimation of fluorescence signal levels

In this section, we calculate the excitation rate of N_2^+ due to the electron beam. Using this excitation rate, we can calculate the expected fluorescence emission rate from the excited N_2^+ ions and calculate the expected signal levels for the optical imaging system used to measure the gas density and temperature.

The excitation rate of N_2 molecules from the ground state to the $B^2\Sigma_u^+$ state of N_2^+ due to energetic electrons from the electron beam is given by:[16]

$$W_{00} = n_e v_e Q_{00}(v_e) , \qquad (7.2.2)$$

where n_e is the electron number density, v_e is the velocity of the primary electrons, and $Q_{00}(v_e)$ is the cross-section for excitation of ground-state N_2 to the $B^2\Sigma_u^+$ state of N_2^+ (vibrational ground state).

The excitation cross-section for 10-keV electrons is $Q_{00}(10 \text{ keV}) = 1.5 \cdot 10^{-18} \text{ cm}^2$; the cross-section decreases with increasing electron energy. Note that the electron beam produces N_2^+ in excited vibrational states as well as in the vibrational ground state. The modeling of the N_2^+ emission spectra discussed in the Flight Experiment Study and Evaluation Section takes this fact into account, and we need only to calculate the excitation rate, W_{00}, to predict the emission intensity from any of the bands, as long as we use the relative emission intensities derived in the Flight Experiment Study and Evaluation Section.

The electron number density in the electron beam is equal to:

$$n_e = \frac{i}{A e v_e} , \qquad (7.2.3)$$

where i is the electron beam current, A is the electron beam cross-sectional area, and e is the electronic charge ($e = 1.6 \cdot 10^{-19}$ coulombs). For number densities $<10^{16} \text{ cm}^{-3}$, quenching effects are negligible. Therefore, the only depopulation mechanism is fluorescence. Since the electron beam excitation probabilities are much smaller than the spontaneous emission probabilities ($W_{ij} \ll A_{ij}$), the fluorescence emission rate per unit volume, N_{fl}, is related to the N_2 gas density, N_g, by:

$$N_{fl} = W_{00} N_g .$$ (7.2.4)

The photometric throughput, P (photoevents, s-1), of an optical imaging system is given by:

$$P = B_\lambda A_d \Omega \eta_{os} \eta_d ,$$ (7.2.5)

where B_λ is the source brightness (photons s^{-1} cm^{-2} ster^{-1}), A_d is the area of the photodetector, Ω is the solid angle of the collection optics for the detector, η_{os} is the overall efficiency of the optical system, and η_d is the quantum efficiency of the detector.

The solid angle, Ω, is related to the f/# of the optical system by:

$$\Omega = \frac{\pi}{4(f/\#)^2} .$$ (7.2.6)

If the fluorescence is isotropic and the excited column is imaged perpendicular to its axis, then the source brightness is given by:

$$B_\lambda = \frac{N_{fl} d}{16} ,$$ (7.2.7)

where d is the diameter of the electron beam. Combining the preceding relationships, we may express the photometric equation as:

$$P = \frac{i Q N_g A_d \eta_{os} \eta_d}{16 e d (f/\#)^2} .$$ (7.2.8)

Note that the photometric throughput is directly proportional to the electron beam current, the gas density, and the efficiencies of the optical system and detector, and it is inversely proportional to the square of the f/#. The expected ranges of values of the system parameters are summarized in Table 7.2.8. The electron beam current, i, will range from ~10 mA in the laboratory experiments to ~1 mA in the flight experiments. In both cases the electron beam will be ~1 mm in diameter. The overall optical system efficiency, η_{os}, will be 40-60%, depending on the the efficiencies of the diffraction gratings and narrowband interference filters used. The quantum efficiency of commercially available CCD detectors

is 5-30%, depending on the particular wavelength. The optical system f/# will range from an optimistic f/3 to a more likely value of f/10.

We now use Eq. 7.2.8 to calculate the expected signal level for an imaging system with the parameters listed in Table 7.2.9. Using these parameters and a nitrogen gas density of $N_g = 10^{14}$ cm^{-3}, the expected photoevent rate is $P = 1.1 \cdot 10^3$ photoevents s^{-1} (per pixel) for the (0,0) transition at 300 K. At this signal rate, a 50-ms exposure would be required to achieve a signal-to-noise ratio of 1, and a 250-s exposure would be required to saturate a CCD pixel (full well of $2.5 \cdot 10^5$ photoevents). Fortunately, most applications do not require the full spatial resolution of the CCD array, and, in these cases, on-chip pixel summation techniques can reduce the integration time and improve the signal-to-noise ratio. Table 7.2.10 summarizes the optical integration (exposure) times required to achieve a signal-to-noise ratio of 30 and 100 (corresponding to 3% and 1% measurement accuracy, respectively) for three different imaging systems, assuming the measurements are shot-noise limited. For applications that demand the full spatial resolution of the CCD array, integration times of 1 s and 10 s will be required for signal-to-noise ratios of 30 and 100, respectively. For these exposure times, the dark noise of the CCD may begin to degrade the signal-to-noise ratio. If the CCD is cooled to -50°C, the dark noise rate is ~16 electron s^{-1} pixel^{-1}, less than 2% of the expected signal level. However, if the array is only cooled to -20°C, the dark noise rate is ~215 electron s^{-1} pixel^{-1}, over 20% of the signal level. Therefore, cooling the CCD array is essential to obtaining high signal-to-noise data, especially for high-resolution applications. For spatially resolved density and temperature measurements that use unity magnification optics, an area of approximately 45 x 5 pixels can be summed together without any loss of spectral or spatial resolution. This results in optical integration times of 5 ms and 50 ms for signal-to-noise ratios of 30 and 100, respectively. For the imaging spectrograph described above, an area of 6 x 4 pixels could be summed together, resulting in integration times of 40 ms and 0.4 s for signal-to-noise ratios of 30 and 100, respectively.

The preceding calculations show that the signal levels for the electron-beam-excited fluorescence will be high enough to permit use of a bare CCD detector, even though its quantum efficiency may be only 5% at 400 nm. The required optical integration times vary widely, depending on the spatial resolution and signal-to-noise ratio. The CCD array must be cooled to -50°C to minimize the dark noise and permit integration times on the order of seconds. For both the laboratory experiments and the in-flight measurements, the electron beam can be pulsed, effectively creating a shutter for the CCD detector. The dynamic range

of the optical imaging system may be extended by varying the electron-beam pulse length as the gas density changes, to maintain a fairly constant signal level.

Spacecraft Glow

In the discussion above on the estimated fluorescence signal level from electron-beam-excited N_2^+, the only sources of noise considered were CCD readout noise and the dark noise of the CCD. We now consider the effect of the optical environment surrounding SHRV and its effect on the design and performance of the optical imaging systems. Sources of optical noise include background radiation from the sky and spacecraft glow. In addition to these sources of optical noise, density gradients in the boundary layer and thermal gradients in the fused silica window may degrade the images and must be considered in the design of the optical instrumentation.

Visible spacecraft glow was first observed on the Atmospheric Explorer spacecraft,[17,18] and was later observed on Space Shuttle flights.[19,20] Spacecraft glow is a diffuse, continuous spectrum of emission usually seen near surfaces undergoing energetic collisions with the ambient atmosphere. Most of this emission lies between 500 nm and 800 nm, peaking near 700 nm. This glow is thought to consist of radiation from the recombination of O atoms and NO to produce NO_2. In addition, some of the glow may be produced by molecular band emission from OH, NO, and N_2^+. The intensity of the glow depends upon the atomic oxygen concentration, the material on the surface of the spacecraft, and the kinetic energy of the air molecules. Spacecraft glow can be a detrimental source of optical noise for optical experiments on platforms in low-earth orbit (such as the Hubble Space Telescope or optical experiments conducted on the Space Shuttle), and the designs of such experiments must attempt to minimize the interference from the glow.

Fortunately, the spectral region of interest for the SHRV flight experiments (380 nm to 400 nm for N_2^+) should be free from interference from spacecraft glow. Studies of spacecraft glow on the Space Shuttle found very little glow at wavelengths shorter than 500 nm.[20] Furthermore, since the kinetic energy of the air molecules for SHRV velocities will be much less than for low-earth orbit vehicles like the Space Shuttle (~8 km/s), and since the SHRV heat shield will not be catalytic, we would expect even less intensity from the glow. Finally, the imaging spectrograph on the SHRV experiments can be designed to minimize any interference from the diffuse glow by using an entrance slit to exclude light

not coming from the electron-beam-excited column, and baffles to prevent stray scattered light from reaching the CCD detector. (Gated detection of pulsed electron-beam fluorescence and background subtraction can be used to further reduce interference.) If, however, future experiments call for observation of optical signals in the 500-nm to 800-nm region (O_2^+ near 600 nm, for example), the spacecraft glow problem should be examined in greater detail to ensure the success of the experiments.

Data Acquisition

In this section, we discuss some of the characteristics of the CCD detector and its architecture that determine the data acquisition rate, as well as the burden this data rate places on the telemetry system.

The time required to make a spatially and/or spectrally resolved measurement with a two-dimensional CCD detector depends on the optical signal level, the CCD readout format, and the time required to digitize and store the data. In a previous section, we calculated the signal levels for electron-beam fluorescence and showed that required optical integration times for good signal-to-noise ratios vary widely depending on the particular imaging system and its spatial resolution. For most applications, however, the required exposure time does not limit the data acquisition rate. Rather, the enormous quantity of data that can be collected with a two-dimensional CCD array (about 220,000 pixels in a typical array) limits the data acquisition rate. Fortunately, proper design of the CCD format can minimize both the data acquisition time and the amount of data that must be transmitted to the ground during the experiment.

A two-dimensional CCD detector, shown schematically in Fig. 7.2.5, consists of a rectangular array of photosensitive sites, or pixels, that produce and store photoelectrons when exposed to light. The number of photoelectrons produced at any pixel is proportional to the integrated light intensity at that site. Although all of the pixels in a two-dimensional array may be exposed simultaneously, reading the data is a serial process. The CCD array is arranged so that the accumulated photocharge may be moved from one pixel location to the next, operating much like a shift register. To measure the photocharge from any pixel, the charge from that pixel must be moved along the rows and columns of the CCD array until it reaches the output node where the charge is converted to a voltage. Normal readout of a CCD array consists of vertically shifting an entire row of pixels into a special horizontal shift register, and then shifting these pixels horizontally, one at a time, into the

output detector. A vertical shift of an entire row of pixels takes 6 μs, while a horizontal shift of one pixel takes 1.4 μs. The charge detection process consists of two reads (the background first, then the pixel value) followed by an A/D conversion. The entire readout process takes 20 μs/pixel for 14-bit accuracy and 5 μs/pixel for 12-bit accuracy.[21] For a typical array with ~220,000 pixels, this readout process takes about 5 seconds for 14-bit accuracy, or just over 1 second for 12-bit accuracy.

Most of the in-flight measurements will not require the full spatial resolution of the CCD array. For these cases, the use of on-chip data summation and frame transfer techniques can significantly reduce the amount of data collected, and also allow a series of measurements to be made very rapidly, without the time-consuming readout process between measurements. On-chip summation involves shifting the photocharge from a number of adjacent pixels into one pixel (or "super pixel") before the photocharge is detected at the output node. For example, N rows of pixels can be shifted into the horizontal shift register before this register is shifted to the output node, effectively summing the N rows and reducing the output data by a factor of N. This technique is especially useful when the image data consists of spectra dispersed along the horizontal dimension of the array. Since the vertical dimension is parallel to the spectrograph slit, many rows can be summed without reducing the spectral resolution. Even for spatially resolved spectra, some on-chip averaging will be useful. On-chip summation not only reduces the number of pixels to be read (and thus the read time), but also increases the signal-to-noise ratio in low-light-level conditions. The limitations to on-chip summation are the spatial resolution required by the experiment and the saturation level of the pixels. The saturation level of individual pixels is ~$2.5 \cdot 10^5$ photoelectrons. The capacity of the horizontal shift register pixels is ~$5 \cdot 10^5$ electrons,[21] and the capacity of the output node is ~10^6 electrons. The data can be further reduced by pixel summation in the digital memory associated with the CCD camera controller. Although off-chip summation will not reduce the overall read-time for the array, it will reduce the amount of data transmitted to the ground during the flight experiments.

Frame transfer techniques provide another way of saving time during the in-flight experiments. This technique, illustrated in Fig. 7.2.6, involves covering a portion of the CCD array with an opaque mask, and using this masked area as a temporary data storage area. In operation, the imaging area of the array is exposed to light (e.g., with a pulsed electron-beam fluorescence spectrum) during an experimental event. Immediately after exposure, the spectrum is shifted vertically into the storage array. Since a vertical shift of

an entire row takes only 6 µs, the data can be transferred to the storage array much faster that it could be read, digitized, and stored in computer memory. After the spectrum is transferred to the storage area, the next experimental event can be recorded and transferred to the storage array. In this way many spectra can be recorded in rapid succession without the time-consuming readout process between measurements. After the storage array is filled, the entire CCD can be read out. The maximum storage time is limited by the dark current of the CCD, and, if the CCD is cooled sufficiently, storage times of tens of seconds should be possible without significant degradation of the signal-to-noise ratio of the images.

One important aspect of the flight instrumentation is the interface between the CCD camera and the on-board SANDAC computer system. The SANDAC IV, designed around the Motorola MC68000 microprocessor, can accommodate up to 16 CPUs in a single system. At least one commercially available CCD camera system uses the Motorola MC68000 for camera control and data acquisition, and this camera system should be relatively easy to interface to the SANDAC IV. This camera system, the Photometrics device described earlier, provides programmable readout formats such as subarray readout, super pixels, and frame transfer mode. The Photometrics camera system is an ideal starting point for both the development of the optical diagnostics and the development of an interface from the camera to the SANDAC. The cost of the complete camera system is about $23 K.

Conclusions and Recommendations

It appears that the only component for which existing technology will not presently meet SHRV requirements is a miniature, tunable uv laser for spectroscopic measurements of NO and other species. This is nevertheless encouraging, since many useful diagnostic techniques, such as spectrally resolved emission and electron-beam fluorescence, do not rely on lasers. Miniature laser technology is advancing rapidly, and there are several promising prospects for miniature laser sources for laser-induced fluorescence measurements. Nevertheless, research and development of flight-worthy miniature lasers should be an important part of an overall research effort in optical diagnostics.

An imaging spectrograph can be designed to make spatially resolved density, rotational temperature, and vibrational temperature measurements in the hypersonic boundary layer using the electron-beam fluorescence technique. In the following

52

discussion we present a program for designing, testing, and flying an imaging spectrograph for SHRV. Since the development of the imaging spectrograph is intimately related to the electron-beam fluorescence research, their anticipated schedules are identical. Therefore, we will refer to the time line presented in the Flight Experiment Study and Evaluation Section for a breakdown of the schedule.

Like the spectroscopic research, the development of the optical hardware requires simultaneous efforts in laboratory research, wind tunnel test experiments, and development of flight hardware for SHRV. Although these tasks are shown as separate time lines, the activities are highly interdependent, and the overall design process is an iterative procedure involving all of them. Initial concepts should be evaluated in laboratory bench tests. A thorough engineering design of the optical system will then produce a prototype instrument that can be tested in the laboratory and then in wind tunnel tests. Problems discovered in the wind tunnel tests will become the subject of further laboratory investigation and engineering analysis. Finally, the optical instrumentation should be integrated into SHRV.

Laboratory Research: Although imaging spectrographs have been designed and flown before, significant laboratory development will be required to develop an imaging spectrograph for the SHRV program. Initially, the emphasis will be on fabricating an imaging spectrograph for use in the electron-beam diagnostic research. This laboratory instrument will be a test bed for optimizing the optical system and CCD format for the signal levels and imaging geometry involved in the electron-beam fluorescence spectroscopy. Also, software and hardware should be developed to operate the CCD detector, and to collect and process the data. The results of this work will influence the development of the spectroscopic techniques as well as the design of the flight hardware. Likewise, the development path of the imaging spectrograph will change as advances are make in the spectroscopic techniques and detector technology. Finally, prototype spectrographs can be evaluated and calibrated in the laboratory electron-beam setup.

Wind Tunnel Experiments: Wind tunnel experiments provide an excellent bridge between the laboratory research effort and the actual flight experiments. These experiments will provide a realistic evaluation of the performance of the imaging spectrograph as well as an ideal opportunity to measure density and temperatures to complement existing wind tunnel data on SHRV. As outlined in the Flight Experiment Study and Evaluation Section, approximately one year will be required for engineering and design of the optical hardware,

and one year for assembly and testing. After successful laboratory testing, the optical hardware should be evaluated in a series of wind tunnel experiments.

The imaging spectrograph design effort will require a full-time optical design engineer, who will be responsible for the overall instrument definition as well as the detailed specifications of all of the optical components and final testing of the instrument. This engineering design is necessarily multidisciplinary; the optical designer must actively participate in all phases of the instrument development from laboratory research, through the optical design and evaluation, assembly and testing, to wind tunnel testing, and, finally, the flight experiments. In addition, the optical designer should work with outside vendors for the design and fabrication of lenses, mirrors, diffraction gratings, and CCD camera hardware. The optical designer must also oversee the assembly and laboratory testing of the instrument package, and participate in eventual wind tunnel testing and the SHRV flights.

Flight Research: Most of the details of the design (both physical and electrical) of the imaging spectrograph should be validated in the wind tunnel tests, and the instrument should be nearly ready to fly after that time. However, specific details unique to the flight experiments must be worked out. Unlike the wind tunnel tests, the flight experiment package must be fully self-contained; that is, the instrument must rely solely on on-board power (batteries), cooling, and computer hardware for its operation. Therefore, a critical part of the design for the imaging spectrograph is integration of the optical flight package into SHRV. This phase of the project should begin as soon as a preliminary design for the imaging spectrograph and electron-beam gun are finished — probably during the second year of the program. This work involves detailed analysis of the power, cooling, and computational requirements of the instrument package, coupled with the weight and volume constraints imposed by SHRV.

References

1. The miniature nitrogen laser and dye laser were purchased from Laser Science, Inc., 80 Prospect Street, Cambridge, MA 02139.
2. T. Gerber, H. M. J. Bastiaens, and P. J. M. Peters, "A miniature high-power KrF laser excited with a capacitively coupled discharge," IEEE J. Quantum Electron. **QE-21**, 191 (1985).

3. R. C. Sze and E. Seegmiller, "Operating characteristics of a high repetition rate miniature rare-gas halide laser," IEEE J. Quantum Electron. **QE-17**, 81 (1981).

4. A. I. Ferguson, "Optically pumped Q-switched micro-YAG laser," in *Conference on Lasers and Electro-Optics Technical Digest Series 1987*, Vol. 14, p. 206, 1987.

5. M. Kimball-Linne and T. Baer, "Q-switching of diode-pumped solid-state lasers," in *Conference on Lasers and Electro-Optics Technical Digest Series 1987*, Vol. 14, p. 206, 1987.

6. J. J. Smith and C. Ma, "Power scaling of Q-switched laser-diode-pumped Nd:YAG lasers," in *Conference on Lasers and Electro-Optics Technical Digest Series 1987*, Vol. 14, p. 346, 1987.

7. Q-switched miniature Nd:YAG lasers are available from Spectra Physics.

8. M. C. Hutley, in *Diffraction Gratings*, (Academic Press, New York, 1982).

9. J. M. Lerner, J. Flamand, J. P. Laude, G. Passereau, and A. Thevenon, "Diffraction gratings ruled and holographic — a review," Proc. SPIE **240**, 82 (1980).

10. J. M. Lerner, R. J. Chambers, and G. Passereau, "Flat field imaging spectroscopy using aberration corrected holographic gratings," Proc. SPIE **268**, 122 (1981).

11. The imaging spectrograph and gratings were purchased from Instruments SA, Inc. 173 Essex Avenue, Metuchen, NJ 08840.

12. Custom concave holographic gratings are available from American Holographic, 521 Great Road, P.O. Box 1310, Littleton, MA 01460.

13. O. J. Edwards, "Optical Transmittance of Fused Silica at Elevated Temperatures," J. Opt. Soc. Am. **56**, 1314 (1966).

14. C. W. Bates, Jr., "Temperature Dependence of the Absorption Edge of Vitreous Silica," Appl. Opt. **15**, 2976 (1976).

15. E. C. Beder, C. D. Bass, and W. L. Shackleford, "Transmissivity and Absorption of Fused Quartz Between 0.22 mm and 3.5 mm From Room Temperature to 1500°C," Appl. Opt. **10**, 2263 (1971).

16. E. P. Muntz, "The Electron Beam Fluorescence Technique," AGARDograph, Vol. 132, Von Karman Institute, Rhode St. Genese, Belgium, 1965.

17. M. R. Torr, P. B. Hays, B. C. Kennedy, and J. C. G. Walker, "Intercalibration of Airglow Observations With the Atmosphere Explorer Satellite," Planet. Space Sci. **25**, 173 (1977).

18. M. R. Torr, "Optical Emissions Induced by Spacecraft-Atmosphere Interactions," Geophys. Res. Lett. **10**, 114 (1983).

19. B. D. Green, E. Murad, and W. T. Rawlins, "The Nature of the Glow and Its Ramifications on Space Based Observations," in Proceedings of the AIAA 20th

Thermophysics Conference, 19-21 June 1985, Williamsburg, VA, Paper AIAA-85-0910 (1985).

20. S. B. Mende and G. R. Swenson, "Vehicle Glow Measurements on the Space Shuttle," in Proceedings of the AIAA 20th Thermophysics Conference, 19-21 June 1985, Williamsburg, VA, Paper AIAA-85-0909 (1985).

21. Photometrics, Ltd., Tucson, AZ.

Table 7.2.1. Comparison of commercially available nitrogen lasers.

	PRA International, Inc. Nitromite LN103	Laser Science, Inc. VSL 337
Output wavelength (nm)	337.1	337.1
Pulse energy (μJ)	70	100
Pulse length (ns)	0.3	3
Timing jitter (ns)	±2	±30
N_2 flow (l/min)	0.1	sealed
Plasma tube size (inches)	22x8x5	4x3x2
Cost (k$)	8	3

Table 7.2.2. Characteristics of the Laser Science, Inc., nitrogen laser and dye laser.

	Nitrogen laser	Dye laser
Pulse length (ns)	4	4
Pulse Energy (μJ)	100	20
Wavelength (nm)	337	365-950
Linewidth (nm)	0.1	0.1
Jitter (ns)	±50	–

Table 7.2.3. Output wavelengths of excimer lasers.

Laser	Wavelength (nm)
ArF	193
KrCl	222
KrF	248
XeCl	308
XeF	351

Table 7.2.4. Spectrograph camera lens and diffraction grating choices.

Spectrograph Camera Focal Length	Required Diffraction Grating and Order	
	Rotational Spectra ($d\lambda/dx = 0.08$ nm/mm) groove density, order	Vibrational Spectra ($d\lambda/dx = 3.2$ nm/mm) groove density, order
225 mm	2400 g/mm, 20 6000 g/mm, 8	1200 g/mm, 1
350 mm	2400 g/mm, 13 6000 g/mm, 5	800 g/mm, 1
450 mm	2400 g/mm, 10 6000 g/mm, 4	600 g/mm, 1

Table 7.2.5. Specifications of Photometrics, Ltd., two-dimensional CCD camera.

Camera System:	Photometrics CC200
Detector Array:	Thompson CFS TH7882CDA
Format:	384 (horizontal) x 576 (vertical)
Pixel size:	23 μm x 23 μm
Quantum Efficiency:	5% at 400 nm, 30% at 500 nm
Features:	CCD array cooled to -50°C
	software programmable readout format

Table 7.2.6. Specifications of miniature spectrograph.

Spectrograph:	Instruments SA UFS-200 Flat Field Spectrograph
Focal length:	200 mm
F/#:	f/3
Gratings:	200, 300, 600, and 1200 grooves/mm
Slits:	50, 100, 250 μm wide; 1, 3, 5 mm in height

Table 7.2.7. Performance of miniature spectrograph and CCD array.

Groove density (g/mm)	Dispersion (nm/mm)	Dispersion (nm/pixel)	Resolution 50 μm slit (nm)	CCD range (nm)	Grating spectral range (nm)
200	24	0.55	1.2	212.0	200-800
300	16	0.37	0.8	141.3	400-800
600	8	0.18	0.4	70.6	200-400
1200	4	0.09	0.2	35.3	200-1200

Table 7.2.8. Typical ranges of values of electron beam parameters and optical system parameters.

electron beam current, i	1-10 mA
electron beam diameter, d	1 mm
optical system efficiency, η_{os}	40-60%
detector quantum efficiency, η_d	5% at 400 nm, 30% at 500 nm
optical system f/#	f/3 to f/10

Table 7.2.9. Imaging system parameters used for photometric throughput calculation.

i	1 mA
d	1 mm
η_{os}	50%
η_d	5%
A_d	22 µm x 22 µm
f/#	8

Table 7.2.10. Required optical integration time for a bare CCD.

| Imaging System	Detector Area (no. of pixels) (effective slit area)	Integration Time signal-to-noise ratio:	
		30:1	100:1
Single-pixel resolution	1 pixel 22 µm x 22 µm	1 s	10 s
Spatially resolved, unity magnification	45 x 5 pixels 1 mm x 0.1 mm	5 ms	50 ms
Imaging spectrograph, 1:8 image magnification	6 x 4 pixels 0.125 mm x 0.01 mm	40 ms	0.4 s
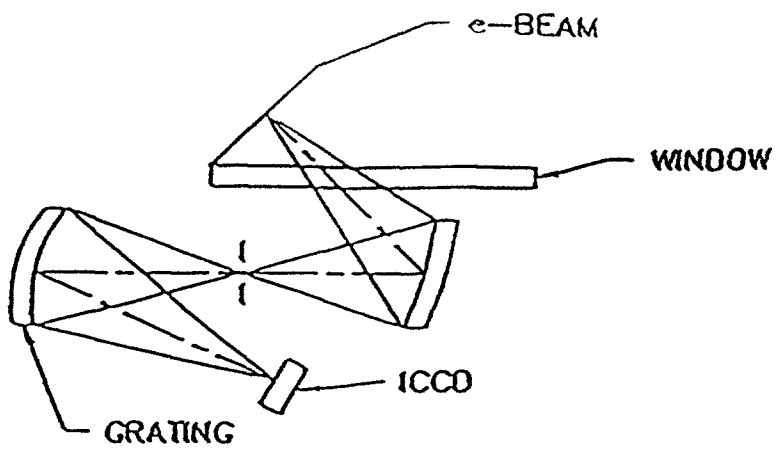
Figure 7.2.1. Imaging Spectrograph.
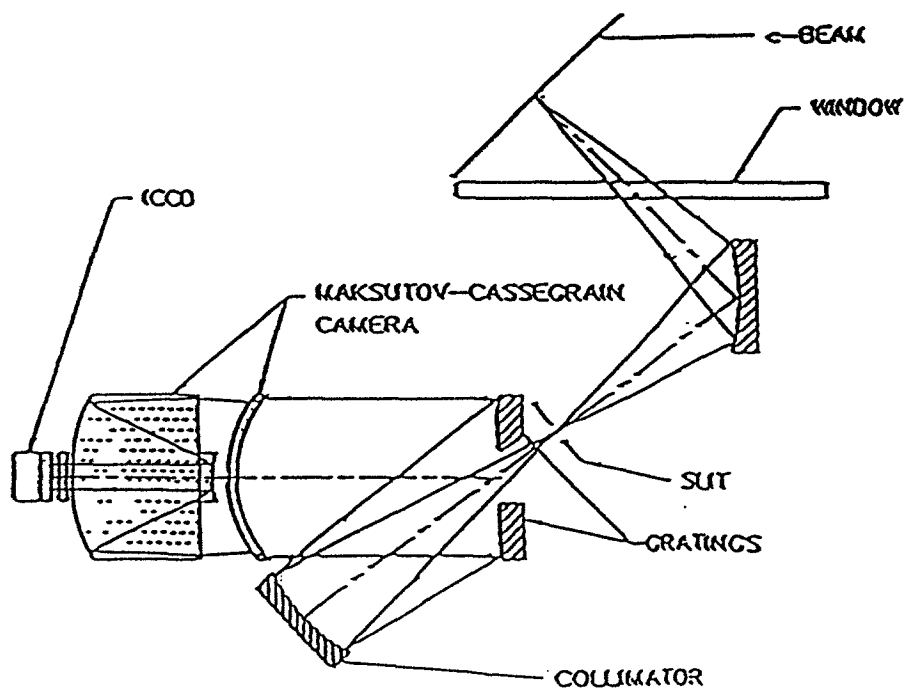
Figure 7.2.2. Dual-grating imaging spectrograph.

ROTATIONAL SPECTRA

8.5 mm
425 pixels

VIBRATIONAL SPECTRA

SLIT
IMAGES

12.5 mm
600 pixels
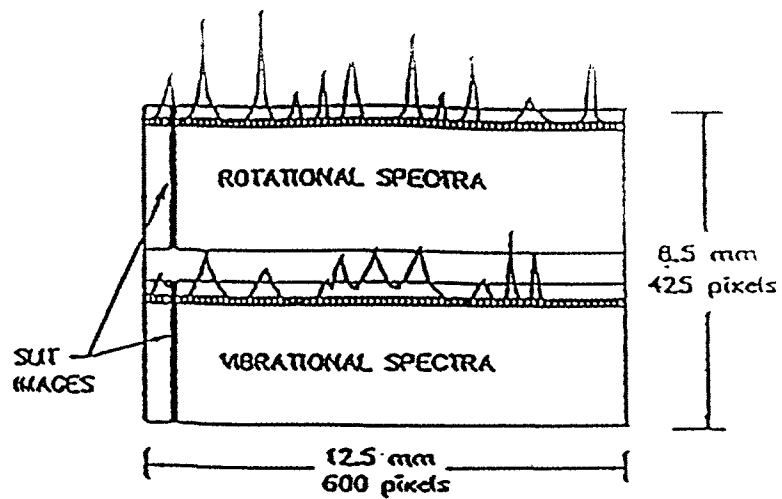
Figure 7.2.3. ICCD detector format.

SLIT

CCD

FLAT FIELD SPECTROGRAPH

~ 11 "
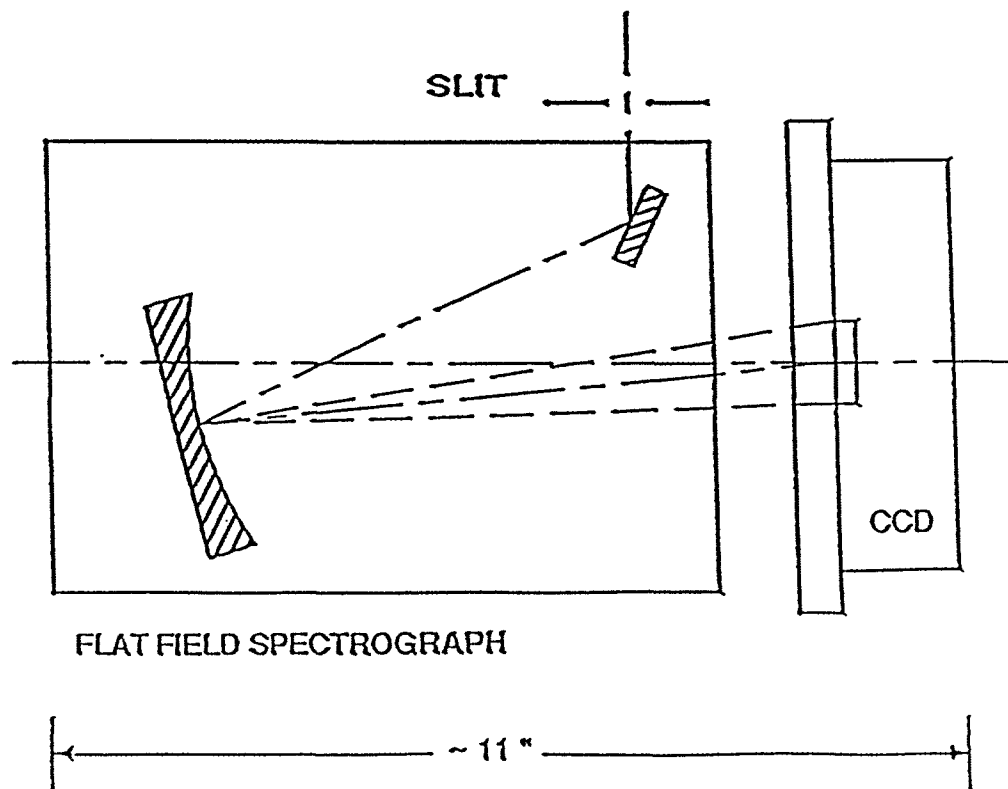
Figure 7.2.4. Schematic diagram of imaging spectrograph.

63

HORIZONTAL
SHIFT
DIRECTION

OUTPUT
NODE

HORIZONTAL REGISTER

----IMAGE ARRAY-----

VERTICAL
SHIFT
DIRECTION
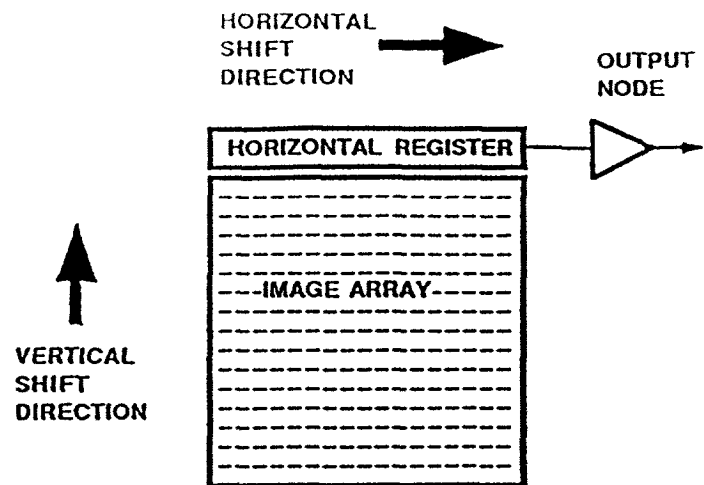
Figure 7.2.5. CCD array architecture.

HORIZONTAL
SHIFT
DIRECTION

OUTPUT
NODE

HORIZONTAL REGISTER

STORAGE
ARRAY

OPAQUE
MASK

IMAGE ARRAY

VERTICAL
TRANSFER
OF PIXELS
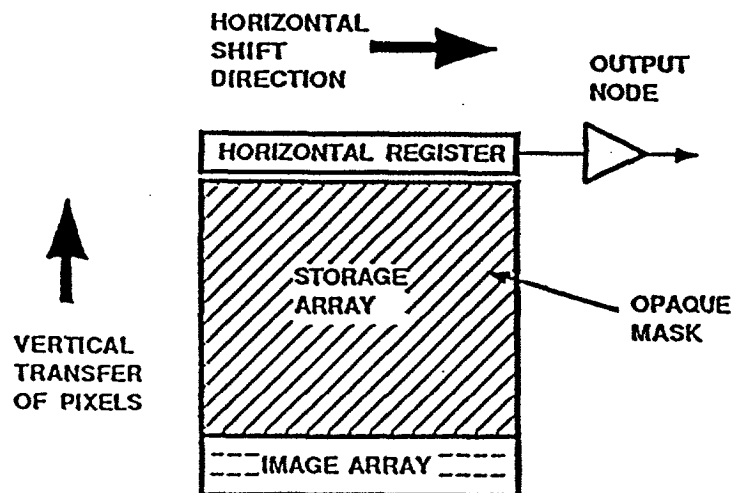
Figure 7.2.6. CCD frame transfer architecture.

64

Bibliography

The following references were useful in the preparation of this feasibility study:

Spectrograph Design:

1. J. F. James and R. S. Sternberg, *The Design of Optical Spectrometers*, (Chapman and Hall Ltd., New York, 1969).
2. R. J. Meltzer, "Spectrographs and Monochromators," in *Applied Optics and Optical Engineering*, *Vol. V*, edited by R. Kingslake (Academic Press, New York, 1969).
3. E. G. Loewen, "Diffraction Gratings, Ruled and Holographic," in *Applied Optics and Optical Engineering*, *Vol. IX*, edited by R. R. Shannon and J. C. Wyant (Academic Press, New York, 1983).
4. J. M. Lerner, R. J. Chambers, and G. Passereau, "Flat Field Imaging Spectroscopy Using Aberration Corrected Holographic Gratings," Proc. SPIE **268**, 122 (1981).
5. M. C. Hutley, *Diffraction Gratings*, (Academic Press, New York,1982).
6. J. M. Lerner, J. Flamand, J. P. Laude, G. Passereau, and A. Thevenon, "Diffraction Gratings Ruled and Holographic — A Review," Proc. SPIE **240**, 82 (1980).

CCDs and Intensifiers:

1. E. L. Dereniak and D. G. Crowe, *Optical Radiation Detectors*, (John Wiley and Sons, New York, 1984).
2. I. P. Csorba, *Image Tubes*, (Howard W. Sams, Inc., Indianapolis,1985).
3. R. K. Chang and M. B. Long, "Optical Multichannel Detection," in *Light Scattering in Solids II*, edited by M. Cardona and G. Guntherodt (Springer-Verlag, New York, 1982).

Spectroscopy:

1. E. P. Muntz, "The Electron Beam Fluorescence Technique," AGARDograph **132**, (1968).

Optical System Design and Lens Design:

1. R. Kingslake, *Lens Design Fundamentals*, (Academic Press, New York, 1978).
2. W. J. Smith, *Modern Optical Engineering*, (McGraw-Hill, New York, 1966).
3. M. Born and E. Wolf, *Principles of Optics*, (Pergamon Press, New York, 1980).
4. L. D. Lorah and E. Ruben, "Aerodynamic Influences on Infrared System Design," in *The Infrared Handbook*, edited by W. L. Wolfe and G. J. Zissis (Environmental Research Institute of Michigan, Ann Arbor, MI, 1985).

Miniature Laser Technology:

1. T. Gerber, H. M. J. Bastiaens, and P. J. M. Peters, "A Miniature High-Power KrF Laser Excited with a Capacitively Coupled Discharge," IEEE J. Quantum Electron. **QE-21**, 191 (1985).
2. R. C. Sze and E. Seegmiller, "Operating Characteristics of a High Repetition Rate Miniature Rare-Gas Halide Laser," IEEE J. Quantum Electron. **QE-17**, 81 (1981).
3. A. I. Ferguson, "Optically Pumped Q-Switched Micro-YAG Laser," in *Conference on Lasers and Electro-Optics Technical Digest Series 1987, Vol. 14*, p. 206 (1987).
4. M. Kimball-Linne and T. Baer, "Q-Switching of Diode-Pumped Solid-State Lasers," in *Conference on Lasers and Electro-Optics Technical Digest Series 1987, Vol. 14*, p. 206 (1987).
5. J. J. Smith and C. Ma, "Power Scaling of Q-Switched Laser-Diode-Pumped Nd:YAG Lasers," in *Conference on Lasers and Electro-Optics Technical Digest Series 1987, Vol. 14*, p. 346 (1987).
6. R. S. Kunabenchi, M. R. Gorbal, and M. I. Savadatti, "Nitrogen Lasers," Prog. Quantum Electron. **9**, 259 (1984).

UNLIMITED RELEASE

INITIAL DISTRIBUTION

J. Larry Howard
Boeing Aerospace Company
P. O. Box 3999
Seattle, WA 98124

Douglas H. Ilgenfritz
Boeing Aerospace Company
P. O. Box 3999
Seattle, WA 98124

T. C. Nark
Boeing Aerospace Company
P. O. Box 3999
Seattle, WA 98124

Dr. David Taylor
MS J567
Los Alamos National Laboratory
Los Alamos, NM 87544

Dr. Robert McKenzie
NASA Ames
Moffett Field, CA 94035

Rodney Bogue
NASA Ames-Dryden, Code OFA
P. O. Box 273
Edwards, CA 93523-5000

Lawrence Reardon
NASA Ames-Dryden Flight
   Research Center
Edwards, CA 93523-5000

Dave Weaver
AFAL
LSCC
Edwards AFB, CA 93523-5000

Richard F. Hellbaum
MS 471
NASA Langley
Hampton, VA 23665-5225

Stuart Ocheltree
MS 235A
NASA Langley
Hampton, VA 23665-5225

James Youngblood
MS 365
NASA Langley
Hampton, VA 23665-5225

Robert C. Anderson
NASA Lewis
21000 Brookpark Road
Cleveland, OH 44135

Robert J. Baumbick
NASA Lewis
21000 Brookpark Road
Cleveland, OH 44135

Dr. Timothy Parr
Naval Weapons Center
China Lake, CA 93555-6001

Bill Yanta
Naval Surface Weapon Center
Code K24
Silver Spring, MD 20910

Lt. Col. Ted Wierzbanowski
Director of Flight Development
NASP Joint Project Office
Wright Patterson AFB
Dayton, OH 45433

Captain Dave Sutton
AFSC/NAT
Wright Patterson Air Force Base
Dayton, OH 45433

Peter Erbland
Air Force Wright Aeronautical
Laboratory/FIMG
Wright Patterson AFB
Dayton, OH 45433

Richard Jacobs
AFWAL/FIGLB
Wright Patterson Air Force Base
Dayton, OH 45433

Walter Sefic
AFSC/NAX
Wright Patterson Air Force Base
Dayton, OH 45433

W. K. McGregor
          Attn: Chad Limbaugh
                    Heard Lowry
Sverdrup Technology
AEDC Group
MS 900 Bldg. 1099
Arnold AFB, TN 37389

Dr. Richard Cusick
Applied Physics Laboratory
Johns Hopkins University
Laurel, MD 20707

Ken Barnes
General Dynamics Corporation
P. O. Box 85357
San Diego, CA 92138

Richard S. Crooks
General Dynamics
P. O. Box 85357
San Diego, CA 92138

Tom Love
General Dyanmics
P. O. Box 85357
San Diego, CA 92138

Dean Wadsworth
General Dynamics
P. O. Box 85357
San Diego, CA 92138

Harold Nakoaka
Marquardt Company
16555 Saticoy Street
Van Nuys, CA 93021

Terri Moseley
McDonnell Aircraft Company
P. O. Box 516
St. Louis, MO 63166

Dr. Bill Watkins
Pratt & Whitney Aircraft
P. O. Box 109600
MS 715-83
West Palm Beach, FL 33410

Sarkis Barkhoudarian
Rocketdyne Division
6633 Canoga Avenue
Canoga Park, CA 91303

Kevin Bowcutt
Rockwell International
MS/WA40
2770 East Carson Street
Lakewood, CA 90712

Dr. Gregory Dobbs
United Technologies Research Center
Silver Lane
MS 90
East Hartford, CT 06108

20	O. E. Jones
1000	V. Narayanamurti
	Attn: F. L. Vook, 1100
	J. P. VanDevender, 1200
	E. H. Barsis, 1400
	W. Herrmann, 1500
	R. J. Eagan, 1800
6000	D. L. Hartley
8000	J. C. Crawford
	Attn: E. E. Ives, 8100
	R. J. Detry, 8200
	R. C. Wayne, 8400
	P. E. Brewer, 8500
8245	R. L. Kee
8300	P. L. Mattern
8310	R. W. Rohde
8340	W. Bauer
8341	M. I. Baskes
8342	M. Lapp
8343	R. H. Stulen
8347	K. L. Wilson
8350	J. S. Binkley
8351	R. P. Lucht
8353	G. A. Fisk
8354	R. E. Palmer
8354	R. J. Cattolica (25)
8357	R. W. Carling
8360	W. J. McLean
8361	D. R. Hardesty
8362	T. M. Dyer
8363	B. R. Sanders
8364	S. C. Johnston
9000	R. L. Hagengruber
9100	R. G. Clem
9140	D. J. Rigali
9142	A. C. Bustamante
9142	G. F. Wright, Jr.
8535	Publications for OSTI (10)
8535	Publications Division/ Technical Library Processes Division, 3141
3141	Technical Library Processes Division (3)
8524-2	Central Technical Files (3)

68